Upward Vertical Two-Phase Flow Through an Annulus—Part II: Modeling Bubble, Slug, and Annular Flow

E. F. Caetano[1]

O. Shoham

J. P. Brill

The University of Tulsa, Tulsa, OK 74104

Mechanistic models have been developed for each of the existing two-phase flow patterns in an annulus, namely bubble flow, dispersed bubble flow, slug flow, and annular flow. These models are based on two-phase flow physical phenomena and incorporate annulus characteristics such as casing and tubing diameters and degree of eccentricity. The models also apply the new predictive means for friction factor and Taylor bubble rise velocity presented in Part I. Given a set of flow conditions, the existing flow pattern in the system can be predicted. The developed models are applied next for predicting the flow behavior, including the average volumetric liquid holdup and the average total pressure gradient for the existing flow pattern. In general, good agreement was observed between the experimental data and model predictions.

Introduction

Part I of this study presented experimental data and analyses of single-phase friction factor, Taylor bubble rise velocity, and flow pattern transition boundaries for concentric and eccentric annuli configurations.

The prediction of liquid holdup and pressure gradient in multiphase flow has been accomplished in the past mainly through correlations. These correlations are developed empirically from experimental data and the majority of them make predictions without taking into account the existing flow pattern. Prediction of liquid holdup and pressure gradient in annuli has followed two approaches: applying correlations originally developed for flow in pipes using the hydraulic diameter concept; or, applying correlations developed from data obtained from two phase flow in an annulus. Empirical correlations for the prediction of pressure gradients in annuli configurations were presented by Baxendell (1958), Gaither et al. (1963), Angel and Welchon (1964) and Winkler (1968). All of these correlations are flow pattern independent, except the Winkler correlation, which is primarily for slug flow conditions. Ros (1961) proposed a method for the prediction of both liquid holdup and pressure gradient based on dimensional analysis and experimental data.

No comprehensive development of mechanistic models covering all possible flow patterns in two-phase flow through an annulus has been attempted. Limited studies with partial flow pattern consideration include the developments by Sadatomi et al. (1982) for vertical flow and Salcudean et al. (1983) and Salcudean et al. (1983) for horizontal flow.

In annular flow through annuli, liquid films exist on both the inner pipe outside wall and on the outer pipe inside wall. Liquid entrainment and deposition takes place between the two films and the gas core. The outside film is normally thicker than the inner one, as found by Andersen and Würtz (1981). Various studies attempted to analyze the process of entrainment/deposition for this configuration. Anderson and Würtz applied pure radiation theory in their analysis, but could not explain the different rates of entrainment for the two films. Using the same radiation approach and the entrainment mechanism suggested by Hutchinson and Whalley (1973), Whalley and Hutchinson (1981) were able to predict different rates of entrainment for the two films. Whalley (1977) provided more insight on the process of entrainment when more than one film exists.

The major mechanisms governing the process of deposition of electrically neutral liquid particles over a surface, as a function of the particle size, were reported by Gardner (1975). The smallest size particles are deposited by a diffusion process. Deposition under the diffusion mechanism for an annulus geometry was investigated by James and Hutchinson (1979). When a particle reaches a certain size, its inertia becomes considerable and the mechanism here is the so-called diffusion impaction. For still larger size particles, the inertia becomes so large that the particles cannot attain the eddy velocity. The deposition rate then falls, and the mechanism is called turbulent impaction. This region was covered in the work by Hutchinson et al. (1971).

The objective of this study is to develop mechanistic models for all possible flow patterns in annuli configurations. This includes bubble, dispersed bubble, slug and annular flow. The

[1] Presently with Petrobras, Rio de Janeiro, Brazil.

Contributed by the Petroleum Division for publication in the JOURNAL OF ENERGY RESOURCES TECHNOLOGY. Manuscript received by the Petroleum Division, September 15, 1990; revised manuscript received June 23, 1991.

models incorporate predictive means for frictional losses and Taylor bubble rise velocity presented in Part I of the study. The models can be applied to predict the flow behavior, mainly the average liquid holdup and pressure gradient. Finally, comparison between experimental data and model prediction is carried out for checking the validity of the proposed models.

Bubble Flow

The bubble flow pattern is characterized by a discontinuous gas phase which is distributed as discrete bubbles rising through a continuous liquid phase. These discrete gas bubbles tend to be spherical in shape and exhibit slippage through the liquid phase due to the buoyancy forces. The bubble flow pattern occurs at low superficial gas velocities with low to medium superficial liquid velocities.

Experimental Holdup and Pressure Gradient Data. The experimental data collected for air-water and air-kerosene bubble flow in a concentric annulus is given in Table 1 in the Appendix. Included are the average volumetric liquid holdup and the total pressure gradient, along with the superficial phase velocities. Similarly, Table 2 shows the data acquired for air-water bubble flow in a fully eccentric annulus.

The data presented in Tables 1 and 2 show considerable differences in liquid holdup and pressure gradient, as the data were acquired over a wide range of superficial velocities. No major differences are observed between the air-water and air-kerosene data, due to similar values of viscosity and density. Also, no major differences are observed between the two configurations, i.e., concentric or fully eccentric annulus. The geometrical configuration mainly affects the frictional losses, which are relatively minor for the bubble flow pattern.

Bubble Flow Model. The basic concept for modeling the bubble flow pattern is the slippage which takes place between the gas and the liquid phases, given by

$$V_S = V_G - V_L = \frac{V_{SG}}{1-H_L} - \frac{V_{SL}}{H_L} \tag{1}$$

The rise velocity of a discrete bubble in a bubble swarm medium is given by

$$V_0 = V_{0,\infty} H_L^n = 1.53 \left[\frac{(\rho_L - \rho_G) g \sigma}{\rho_L^2} \right]^{1/4} H_L^n \tag{2}$$

where $V_{0,\infty}$ is the solitary bubble rise velocity in an infinite medium given by Harmathy (1955), and H_L^n is a correction for the bubble swarm effect suggested by Wallis (1969). A value between 1 to 2 for the index n was recommended by Wallis, to account for the reduction of the density of the medium which tends to decrease the bubble rise velocity. However, another three-dimensional effect takes place, which tends to increase the bubble rise velocity. This effect occurs due to the entrainment of bubbles in each other's wake. Thus, the index n is expected to be less than unity. Indeed, as mentioned by Fernandes et al. (1983), a value of $n = 0.5$ seems to better match the experimental data.

Combining Eqs. (1) and (2) and rearranging yields

$$H_L^{n+2} - H_L^{n+1} + \frac{(V_{SL}+V_{SG})H_L}{1.53\left[\frac{(\rho_L-\rho_G)g\sigma}{\rho_L^2}\right]^{1/4}} - \frac{V_{SL}}{1.53\left[\frac{(\rho_L-\rho_G)g\sigma}{\rho_L^2}\right]^{1/4}} = 0 \tag{3}$$

which is an implicit equation for the liquid holdup, H_L.

The total pressure gradient for steady-state flow is composed of three components, i.e.,

$$\left(\frac{dp}{dz}\right)_T = \left(\frac{dp}{dz}\right)_G + \left(\frac{dp}{dz}\right)_F + \left(\frac{dp}{dz}\right)_A \tag{4}$$

These components are referred to as the potential energy or

Nomenclature

a = parameter
A = area
B = constant
C = constant; concentration
C_K, C_M = theoretically or experimentally determined indices
(dp/dz) = pressure gradient
D = diameter, deposition rate
DBC = distance between centers of pipes in annulus
e = annulus eccentricity
E = entrainment rate
$\bar{E}$ = average percent error
f = Fanning friction factor
Fe = liquid fraction entrained in gas core
g = acceleration of gravity
G = dimensionless group
h = local holdup
H = in-situ holdup
k = mass transfer coefficient
K = annulus pipe diameter ratio
l = distance from nose of Taylor bubble to given point
L = length
L_C = length of Taylor bubble cap
p = pressure
Q = volumetric flow rate
r = radial position coordinate
Re = dimensionless Reynolds no.
S = liquid wetted perimeter
T = tubing film to casing film thickness ratio
$\mathcal{V}$ = volume
V = local or in-situ velocity
W = solid angle
X_M = dimensionless modified Lockhart-Martinelli parameter
Y_M = dimensionless inclination group
z = vertical distance
δ = liquid film thickness
λ = nonslip liquid holdup
μ = dynamic viscosity
ρ = density
σ = surface tension; standard deviation
τ = shear stress
ϕ = gas dimensionless no.
θ = integration variable

Subscripts

A = acceleration
C = casing
CI = casing liquid film-core mixture interface
D = deposition
E = entrainment
F = friction
G = gas; gravitation
H = hydraulic
I = interface
L = liquid
LF = liquid film
LS = liquid slug
M = mixture; measured
P = predicted
SG = superficial gas
SL = superficial liquid
S = slip
SU = slug unit
T = tubing; total; translational
TB = Taylor bubble
TI = tubing liquid film-core mixture interface
W = wall
0 = discrete bubble
0, ∞ = free rise of discrete bubble

Superscripts

n = bubble swarm index
N = Nusselt
R = relative
x = exponent in Blasius equation
$\sim$ = normalized or dimensionless variable
$*$ = true value
$'$ = planar
$<>$ = average over cross section

Table 1 Experimental liquid holdup and total pressure gradient in bubble flow—concentric annulus

Test Number	Superficial Gas Velocity (m/s)	Superficial Liquid Velocity (m/s)	Liquid Holdup	Total Pressure Gradient (Pa/m)
air-water				
1	0.037	0.002	0.8750	7003.5
2	0.039	0.004	0.8700	6940.1
3	0.039	0.012	0.8700	7186.0
4	0.051	0.058	0.8700	--------
5	0.040	0.090	0.9000	8859.5
6	0.046	0.229	0.9250	9541.6
7	0.053	0.698	0.9400	9993.7
8	0.069	0.887	0.9350	10707.6
9	0.061	0.024	0.8050	6741.8
10	0.060	0.062	0.8175	6995.6
11	0.059	0.111	0.8375	7209.8
12	0.064	0.116	0.8535	7495.3
13	0.064	0.329	0.9050	7772.9
14	0.068	0.162	0.8615	--------
15	0.076	0.498	0.9100	--------
16	0.101	0.999	0.9125	--------
17	0.158	1.196	0.8600	--------
18	0.245	1.449	0.8035	8986.4
19	0.283	1.954	0.7810	9053.8
20	0.141	0.992	--------	9133.2
21	0.013	0.095	--------	8447.1
22	0.013	0.002	--------	8090.2
23	0.021	0.997	--------	9160.9
air-kerosene				
24	0.040	0.003	0.8150	--------
25	0.040	0.005	0.8230	--------
26	0.041	0.012	0.8170	--------
27	0.042	0.041	0.8335	--------
28	0.042	0.112	0.8980	--------
29	0.059	0.397	0.9940	--------
30	0.062	0.698	0.9600	--------
31	0.049	0.003	0.7650	--------
32	0.052	0.040	0.7975	--------
33	0.056	0.405	0.9300	--------
34	0.075	0.698	0.9600	--------
35	0.075	0.109	0.8000	--------
36	0.108	0.708	0.9275	--------
37	0.252	0.708	0.8050	--------
38	0.261	1.007	0.8500	
39	0.658	1.197	0.7215	6424.5
40	0.485	1.196	--------	6840.9
41	0.244	0.798	0.8400	7110.6
42	0.086	0.399	0.8950	7138.4
43	0.050	0.100	0.8475	6753.7
44	0.056	0.349		7348.6
45	0.032	0.003	0.7600	6305.6
46	0.030	0.010	0.8450	6488.0
47	0.029	0.035	0.8950	7019.4
48	0.029	0.188	0.7950	7614.3
49	0.029	0.294	--------	7765.0
50	0.044	0.698	--------	8121.9
51	0.037	0.698	0.9600	8062.4

Table 2 Experimental liquid holdup and total pressure gradient in bubble flow—fully eccentric annulus

Test Number	Superficial Gas Velocity (m/s)	Superficial Liquid Velocity (m/s)	Liquid Holdup	Total Pressure Gradient (Pa/m)
air-water				
1	0.039	0.003	0.9280	7138.5
2	0.036	0.003	0.9290	7138.5
3	0.037	0.005	0.9295	7138.5
4	0.037	0.008	0.9295	7138.5
5	0.038	0.012	0.9285	7138.5
6	0.039	0.033	0.9355	7138.5
7	0.041	0.051	0.8780	6741.9
8	0.042	0.082	0.8995	6741.9
9	0.041	0.165	0.9150	7138.5
10	0.042	0.387	0.9410	7138.5
11	0.068	0.798	0.9360	7931.7
12	0.030	0.004	0.9020	7138.5
13	0.032	0.007	0.9140	7138.5
14	0.031	0.012	0.9040	7138.5
15	0.026	0.033	0.9405	7535.1
16	0.026	0.051	0.9240	7535.1
17	0.023	0.092	0.9390	7138.5
18	0.120	0.977	0.9055	9696.5
19	0.141	1.436	0.9135	9993.9
20	0.186	1.246	0.8820	9637.0
21	0.184	1.565	0.8810	9934.4
22	0.187	1.994	0.9010	10231.9
23	0.245	1.994	0.8850	9934.4
24	0.241	2.512	0.8910	10553.1
25	0.127	1.515	0.9265	10184.3

gravity losses, the friction losses, and the kinetic energy change or convective acceleration losses, respectively.

Successful modeling of two-phase flow pressure gradient requires analyzing each component as a function of the existing flow pattern. The gravitation pressure gradient is evaluated through the slip density, ρ_S, based on the in-situ liquid holdup. Thus, the gravitation component is given by

$$\left(\frac{dp}{dz}\right)_G = \rho_S g \tag{5}$$

where

$$\rho_S = \rho_L H_L + \rho_G (1 - H_L) \tag{6}$$

and the in-situ liquid holdup, H_L, is given by Eq. (3).

The acceleration pressure gradient in bubble flow is normally negligible. Thus,

$$\left(\frac{dp}{dz}\right)_A = 0 \tag{7}$$

The friction pressure gradient component is evaluated applying the Fanning friction factor for annuli configurations.

$$\left(\frac{dp}{dz}\right)_F = \frac{4f}{D_H}\rho_S \frac{V_M^2}{2} \tag{8}$$

where the mixture velocity, V_M, is given by

$$V_M = V_{SL} + V_{SG} \tag{9}$$

and the hydraulic diameter is given by

$$D_H = D_C - D_T \tag{10}$$

The Fanning friction factor, f, is determined by the method presented in Part I of this study. The Reynolds number for bubble flow is defined by

$$\mathrm{Re}_S = \frac{\rho_S V_M D_H}{\mu_M} \tag{11}$$

The mixture viscosity, μ_M, after Dukler et al. (1964), is given by

$$\mu_M = \mu_L \lambda_L + \mu_G (1 - \lambda_L) \tag{12}$$

where the non-slip liquid holdup λ_L is

$$\lambda_L = \frac{V_{SL}}{V_{SL} + V_{SG}} \tag{13}$$

Combining Eqs. (4), (5), (7), and (8), the total pressure gradient for bubble flow is

$$\left(\frac{dp}{dz}\right)_T = \rho_S g + \frac{4f}{(D_C - D_T)}\rho_S \frac{(V_{SL} + V_{SG})^2}{2} \tag{14}$$

Evaluation of Bubble Flow Model. The model for bubble flow was used to predict the liquid holdup and total pressure gradient for the experimental flow conditions given in Tables 1 and 2. The performance of the model was obtained by comparing the predicted results with measured data. This performance is reported in terms of the average percent error, $\bar{E}$, and the percent standard deviation, σ.

Figures 1 and 2 show the model performance for the average volumetric liquid holdup prediction in the concentric and fully eccentric annulus, respectively. These predictions were made with a value of 0.5 for the index n in Eq. (3). This value of 0.5 gave the best agreement between the experimental and predicted results. The performance obtained with the model is very good, with a slight underprediction tendency of less than 3.0 percent. The degree of scatter about the mean is also good, with a standard deviation of less than 5.0 percent. In general, the model performs very good, independent of either physical properties or annulus configuration.

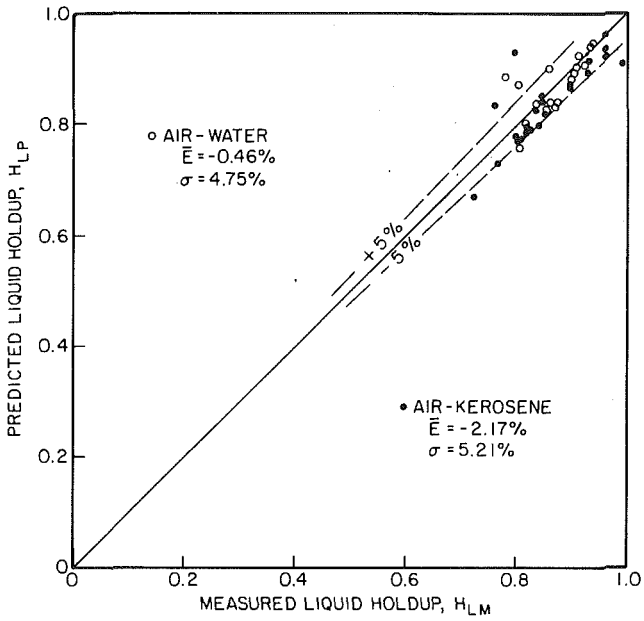

Fig. 1 Bubble flow model performance—average volumetric liquid holdup in concentric annulus

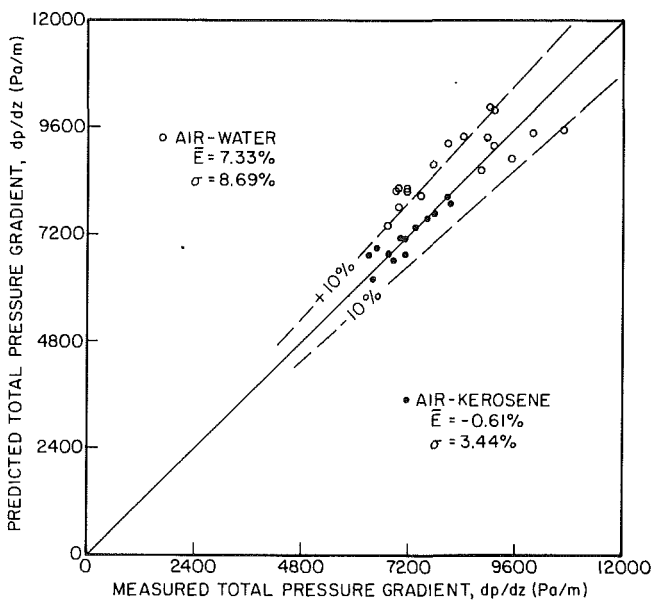

Fig. 3 Bubble flow model performance—total pressure gradient in concentric annulus

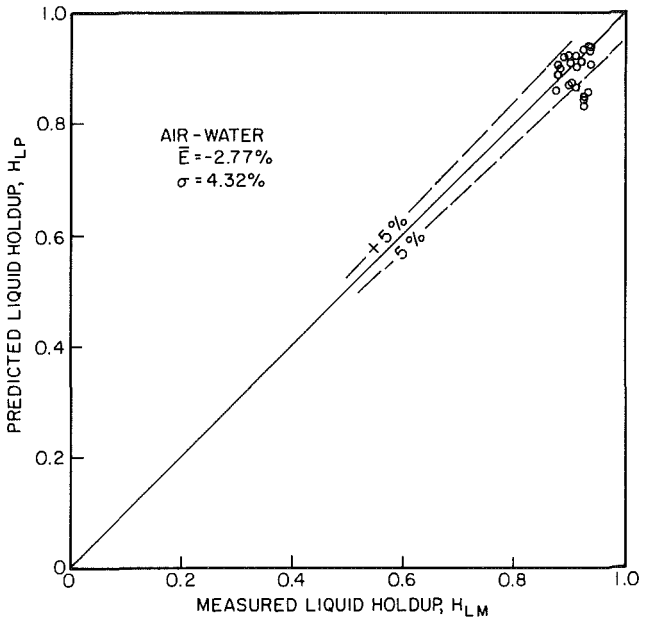

Fig. 2 Bubble flow model performance—average volumetric liquid holdup in fully eccentric annulus

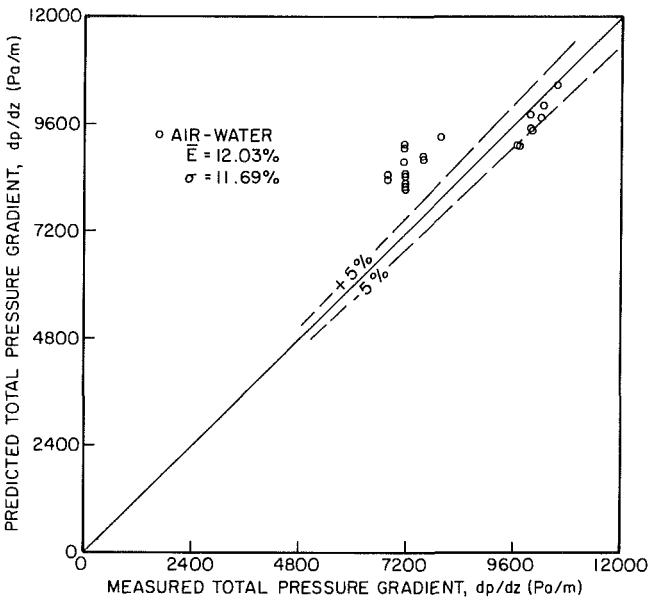

Fig. 4 Bubble flow model performance—total pressure gradient in fully eccentric annulus

Figures 3 and 4 show the model performance for the total pressure gradient prediction in the concentric and fully eccentric annulus, respectively. The agreement between the model and experimental results is good, showing an acceptable average error and degree of scatter. Figure 4 shows the agreement is weaker for the fully eccentric annulus case, with average percent error and standard deviation values of slightly over 10 percent. This was caused by the very low superficial phase velocities used when acquiring the data in this configuration. Under these conditions the flow is sometimes unstable, due to a heating phenomena, which can cause a lower degree of measurement accuracy.

Dispersed Bubble Flow

The dispersed bubble flow pattern occurs at low to medium superficial gas velocities with high superficial liquid velocities. This flow pattern is characterized by a discontinuous gas phase, which is distributed as spherical discrete bubbles in a continuous liquid phase. These discrete gas bubbles do not exhibit significant slippage through the liquid phase, due to the high liquid phase velocities. Thus, dispersed bubble flow can be treated as a no-slip homogeneous mixture flow.

Experimental Holdup and Pressure Gradient Data. The experimental data collected for the average volumetric liquid holdup and the total pressure gradient are given in Tables 3 and 4 in the Appendix. Table 3 shows the data acquired for air-water and air-kerosene in a concentric annulus. Similarly, Table 4 shows the data acquired for air-water in a fully eccentric annulus.

High values of liquid holdup, up to 0.96, are encountered in this flow pattern. These are the highest liquid holdup values

Table 3 Experimental liquid holdup and total pressure gradient in dispersed bubble flow—concentric annulus

Test Number	Superficial Gas Velocity (m/s)	Superficial Liquid Velocity (m/s)	Liquid Holdup	Total Pressure Gradient (Pa/m)
air-water				
1	0.069	1.545	0.9600	11500.7
2	0.057	2.054	0.9600	11500.7
3	0.107	1.515	0.9115	--------
4	0.099	1.834	0.9315	--------
5	0.091	2.991	0.9450	--------
6	0.167	1.874	0.8850	--------
7	0.149	3.051	0.9300	--------
8	0.575	2.991	0.8300	--------
9	0.437	2.293	0.8250	--------
10	1.112	2.881	0.7540	--------
11	0.480	1.984	0.8100	9847.0
12	0.242	2.094	0.8320	9851.0
13	0.155	1.775	--------	10132.5
14	0.020	1.954	--------	10890.0
air-kerosene				
15	0.063	0.997	0.9600	--------
16	0.079	1.007	0.9600	--------
17	0.108	0.997	0.9600	--------
18	0.270	1.515	0.9025	--------
19	0.511	1.495	0.7825	--------
20	0.663	1.515	0.7400	7110.6
21	0.651	2.393	0.8350	8923.0
22	0.484	1.505	--------	7364.4
23	0.478	1.994	0.8450	8328.1
24	1.074	1.994	0.7050	--------
25	1.195	1.994	0.6775	--------
26	0.245	1.994	0.9400	9101.4
27	0.117	1.007	--------	7733.2
28	0.114	1.495	0.9600	8629.5
29	0.113	1.994	0.9600	9339.4
30	0.076	1.191	--------	8419.3
31	0.073	1.495	--------	8804.0
32	0.070	1.994	0.9600	9430.6
33	0.044	1.097	--------	8328.1
34	0.043	1.296	--------	8597.8
35	0.043	1.794	0.9600	9133.2
36	0.040	0.997	0.9600	8328.1

Table 4 Experimental liquid holdup and total pressure gradient in dispersed bubble flow—fully eccentric annulus

Test Number	Superficial Gas Velocity (m/s)	Superficial Liquid Velocity (m/s)	Liquid Holdup	Total Pressure Gradient (Pa/m)
air-water				
1	0.174	2.971	0.9350	11481.1
2	0.224	2.991	0.9150	11243.1
3	0.243	3.001	0.9160	11183.7
4	0.229	3.579	0.9305	11897.5
5	0.383	2.991	0.8670	11064.7
6	0.591	2.951	0.8190	10767.2
7	0.792	3.383	0.7893	11183.7
8	1.079	3.529	0.7530	11421.6
9	0.128	1.994	0.9317	10767.2
10	0.133	2.492	0.9600	11528.7
11	0.139	2.971	0.9600	11897.5

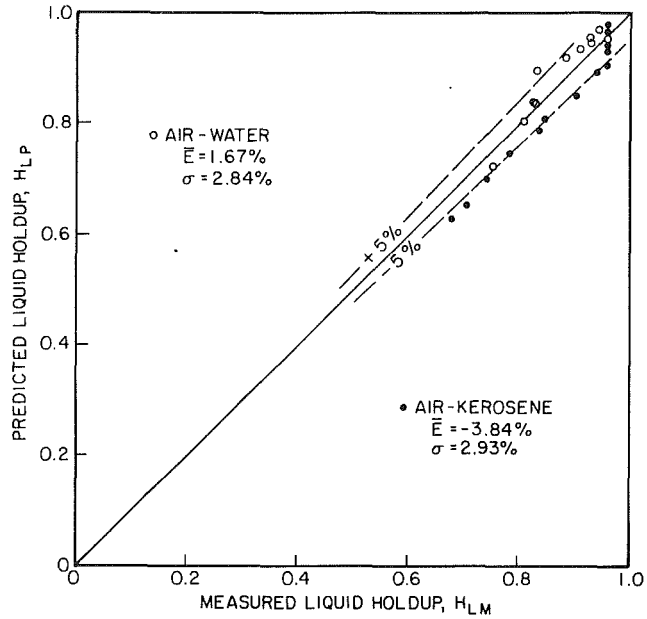

Fig. 5 Dispersed bubble flow model performance—average volumetric liquid holdup in concentric annulus

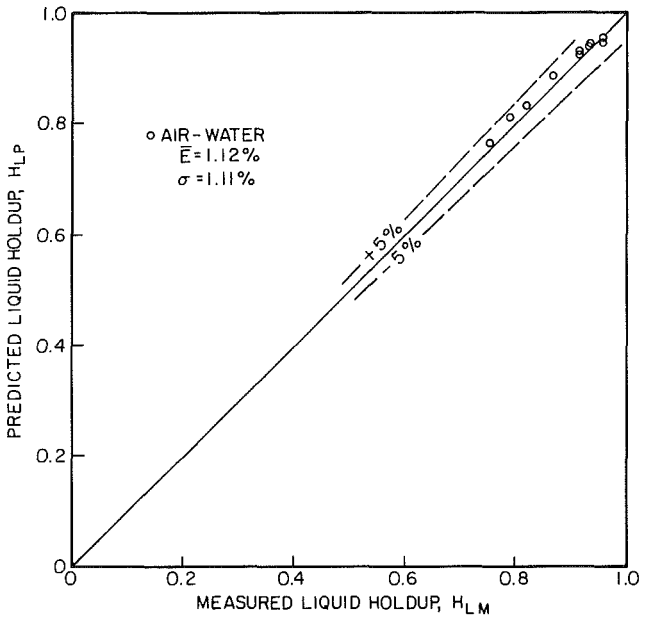

Fig. 6 Dispersed bubble flow model performance—average volumetric liquid holdup in fully eccentric annulus

measured in this study. Although no significant slippage occurs between the two phases, the high liquid holdup values are due mainly to the high liquid velocities needed to establish dispersed bubble flow. Consequently, high gravitation pressure gradients are observed in this flow pattern.

No major differences are observed between the air-water and air-kerosene liquid holdup data. This is expected due to the fairly homogeneous nature of this flow pattern. However, lower values of pressure gradients are encountered in the fully eccentric annulus. This is mainly due to the lower frictional losses occurring in the fully eccentric configuration. This effect is especially significant in dispersed bubble flow, where the friction pressure gradient exhibits the same order of magnitude as the gravitation component.

Dispersed Bubble Flow Model. The basic concept for modeling the dispersed bubble flow pattern is the fairly no-slip, homogeneous nature of this flow. Thus, the in-situ liquid and gas velocities are equal, $V_L = V_G$. Hence, using Eq. (1) and rearranging shows that the in-situ liquid holdup, H_L, is equal to the nonslip liquid holdup, λ_L, as given by Eq. (13). The total pressure gradient is given by

$$\left(\frac{dp}{dz}\right)_T = \rho_M g + \frac{4f}{(D_C - D_T)} \rho_M \frac{(V_{SL} + V_{SG})^2}{2} \tag{15}$$

The two terms of the R.H.S. of Eq. (15) are the gravity losses and friction losses, respectively. The acceleration losses are neglected due to the homogeneous and steady characteristics of the mixture. The mixture density is given by

$$\rho_M = \rho_L \lambda_L + \rho_G (1 - \lambda_L) \tag{16}$$

The Fanning friction factor is determined through the method presented in the Single-Phase Friction Factor section in Part I of this study. The corresponding Reynolds number for this case is as defined by Eq. (11), with ρ_M instead of ρ_S.

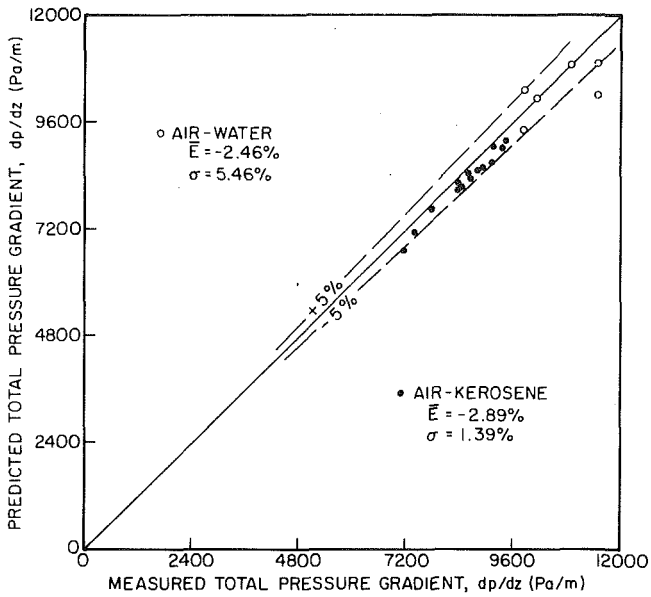

Fig. 7 Dispersed bubble flow model performance—total pressure gradient in concentric annulus

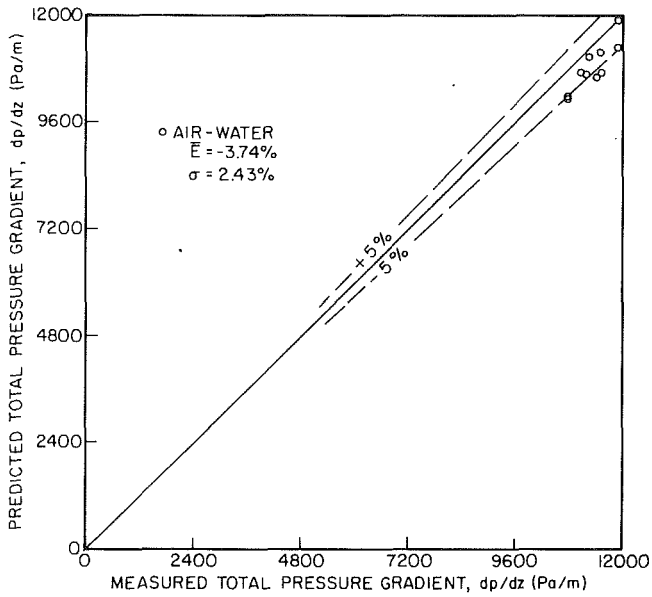

Fig. 8 Dispersed bubble flow model performance—total pressure gradient in fully eccentric annulus

Evaluation of Dispersed Bubble Flow Model. The model for dispersed bubble flow is tested against the experimental data given in Tables 3 and 4.

Figures 5 and 6 show the model performance for the average volumetric liquid holdup prediction in the concentric and fully eccentric annuli, respectively. The performance obtained by the model is very good, with a slight overprediction tendency for air-water flow and an equally slight underprediction tendency for air-kerosene flow. The standard deviation about the mean is below 3.0 percent. The model performs equally well for either fluid pair or annulus configuration.

Similarly, the model performance for the total pressure gradient prediction in the concentric and fully eccentric annulus is given in Figs. 7 and 8, respectively. The agreement between the model and experimental results is again very good, showing low values of average percent error and standard deviation.

Slug Flow

Slug flow occurs over a wide range of flow rates and is one of the most frequently encountered flow patterns in two-phase flow. It is characterized by the alternate flow of gas and liquid. The gas phase appears in two different forms: large bullet-shaped bubbles termed Taylor bubbles, and small spherical bubbles dispersed in the liquid phase. The Taylor bubbles occupy almost the whole configuration cross section and move uniformly upward. The liquid phase appears both in the form of liquid slugs which bridge the pipe cross section and as falling liquid films which flow downward between the Taylor bubbles and pipe walls. The liquid slugs which separate successive Taylor bubbles contain the dispersed small spherical gas bubbles. The complex distribution of the two phases and the intermittent nature of the flow makes modeling slug flow difficult and challenging.

Experimental Holdup and Pressure Gradient Data. The experimental data collected for the average volumetric liquid holdup and the total pressure gradient are given in Tables 5 and 6 for the concentric annulus and for the fully eccentric annulus, respectively.

A wide range of average liquid holdup values was encountered for slug flow. At low superficial liquid velocities, the liquid holdup can have values between 0.2 and 0.8. At medium and high superficial liquid velocities, the range of variation for the liquid holdup narrows to values between 0.45 and 0.80. The wide range of average liquid holdup values encountered in slug flow affects the pressure gradient, which also presents a wide range of values. The pressure gradient in slug flow is the smallest observed as compared to other flow patterns. This can be explained by the relatively low gravitation pressure drop, coupled with low friction losses.

Although no major differences are observed between the air-water and air-kerosene liquid holdup data, air-kerosene shows slightly lower values. This is due to the effect of the different physical properties on the inertia forces and slippage. With respect to pressure gradient, the fully eccentric annulus is expected to have lower friction pressure gradients than a concentric configuration. However, the friction pressure gradient component is approximately one order of magnitude smaller than the gravitation and acceleration components. The net effect of the configurations on the pressure gradient is small and can hardly be identified from the data.

Slug Flow Model. The hydrodynamic model developed for slug flow in annuli takes into account two possible configurations. First, fully developed Taylor bubble flow, occurring when the bubble cap length is negligible as compared to the total liquid film length. Under this condition, the film thickness reaches a constant terminal value which can be used as the average thickness for the entire film zone. Second, a developing Taylor bubble, which consists only of a cap bubble. For this case the film thickness varies continuously along the film zone, and cannot be assumed as constant.

The model developed for the case of a constant film thickness constitutes a simplified form of the model developed by Fernandes et al. (1983) for upward vertical pipe flow. The model has been extended in this study, using the characteristics observed for the slug flow pattern in annuli. For the case of a cap bubble with varying film thickness, the model follows the approach of McQuillan and Whalley (1985), who studied the transition from bubble to slug flow.

The physical model of slug flow is shown schematically in Fig. 9. The figure shows a unit slug, consisting of a Taylor bubble and a film region, followed by an adjacent liquid slug.

Table 5 Experimental liquid holdup and total pressure gradient in slug flow—concentric annulus

Test Number	Superficial Gas Velocity (m/s)	Superficial Liquid Velocity (m/s)	Liquid Holdup	Total Pressure Gradient (Pa/m)
air-water				
1	0.125	0.004	0.6875	--------
2	0.125	0.011	0.7050	--------
3	0.123	0.014	0.7015	--------
4	0.122	0.299	0.8015	--------
5	0.124	0.495	0.8350	--------
6	0.475	0.003	0.5233	--------
7	0.473	0.017	0.5133	--------
8	0.459	0.111	0.5425	--------
9	0.492	1.087	0.7300	--------
10	0.523	1.575	0.7400	--------
11	0.514	1.956	0.7625	--------
12	1.085	0.003	0.3783	--------
13	1.084	0.111	0.4075	--------
14	1.062	1.002	0.5975	--------
15	1.055	2.044	0.7250	--------
16	1.093	2.413	0.7350	--------
17	1.951	1.426	0.5100	--------
18	1.872	2.034	0.5600	--------
19	1.894	2.472	0.5800	--------
20	1.822	2.881	0.6000	--------
21	3.247	1.489	0.3837	--------
22	3.211	1.984	0.4290	--------
23	3.134	2.413	0.4575	--------
24	3.082	2.891	0.4825	--------
25	6.622	1.475	0.3493	--------
26	5.858	2.413	0.4100	--------
27	9.458	1.475	0.2900	--------
28	0.095	0.003	0.7633	--------
29	0.434	0.003	0.4690	4433.7
30	0.455	0.011	0.4965	4461.5
31	0.437	0.101	0.5340	5056.4
32	0.192	0.033	0.5963	5682.9
33	0.203	0.254	0.6690	6753.7
34	0.241	0.279	0.6560	6436.4
35	0.205	0.011	--------	5770.2
36	0.198	0.100	--------	6277.8
37	0.117	0.100	0.7550	7257.4
38	0.114	0.011	--------	6781.5
39	0.115	0.003	--------	6694.2
40	0.409	0.239	--------	5536.2
41	0.407	0.035	--------	4461.5
air-kerosene				
42	0.079	0.003	0.6925	--------
43	0.077	0.012	0.7315	--------
44	0.075	0.042	0.7750	--------
45	0.202	0.003	0.5675	--------
46	0.199	0.109	0.6075	--------
47	0.434	0.003	0.4540	--------
48	0.455	0.705	0.6800	--------
49	0.594	0.003	0.4300	3097.3
50	0.586	0.012	0.4450	3125.0
51	0.592	0.019	0.4445	3125.0
52	0.438	0.003	--------	3331.2
53	0.428	0.012	0.4860	3470.0
54	0.413	0.019	--------	3632.6
55	0.411	0.130	--------	3838.9
56	0.996	0.003	0.3665	--------
57	1.009	0.103	0.4000	--------
58	1.020	1.001	0.5810	--------
59	1.043	1.202	0.6180	--------
60	1.176	1.001	0.5450	--------
61	1.203	1.505	1.6235	--------
62	6.718	0.997	0.2400	--------
63	6.502	1.495	0.3080	--------
64	5.986	1.994	0.3450	--------
65	3.383	0.999	0.3435	--------
66	4.233	0.997	0.3010	--------
67	9.320	0.995	0.2025	--------
68	2.130	0.798	0.3820	--------
69	0.196	0.003	--------	4465.5
70	0.194	0.010	0.5900	4552.7
71	0.191	0.042	0.6200	4584.4
72	0.195	0.112	--------	4731.2
73	0.083	0.042	--------	5742.4
74	0.428	0.042	0.4892	3747.6
75	0.591	0.042	0.4480	3275.7
76	0.313	0.020	0.5150	3957.8
77	0.329	0.199	0.5765	4493.2
78	0.621	0.199	0.4900	3779.4
79	0.993	0.199	0.4225	3244.0

Table 6 Experimental liquid holdup and total pressure gradient in slug flow—fully eccentric annulus

Test Number	Superficial Gas Velocity (m/s)	Superficial Liquid Velocity (m/s)	Liquid Holdup	Total Pressure Gradient (Pa/m)
air-water				
1	0.076	0.003	0.7600	7733.4
2	0.080	0.005	0.7650	7733.4
3	0.080	0.007	0.7800	7792.9
4	0.077	0.010	0.8015	8090.3
5	0.073	0.012	0.8066	7852.4
6	0.081	0.027	0.8065	8149.8
7	0.081	0.052	0.7985	8268.8
8	0.082	0.076	0.8140	8328.3
9	0.076	0.100	0.8285	8387.7
10	0.091	0.003	0.7745	7495.4
11	0.124	0.008	0.7210	6662.6
12	0.124	0.011	0.7135	7079.0
13	0.126	0.028	0.7130	7079.0
14	0.126	0.052	0.7200	7198.0
15	0.129	0.075	0.7245	7257.5
16	0.126	0.099	0.7450	7495.4
17	0.121	0.156	0.7800	7757.2
18	0.168	0.005	0.6625	6484.1
19	0.168	0.008	0.6650	6365.2
20	0.171	0.023	0.6560	6757.8
21	0.170	0.050	0.6600	6599.1
22	0.171	0.075	0.6965	6900.6
23	0.169	0.097	0.7150	7090.9
24	0.170	0.160	0.7300	7317.0
25	0.377	0.005	0.5010	4580.5
26	0.381	0.007	0.5155	4616.2
27	0.317	0.012	0.5370	5151.6
28	0.318	0.019	0.5385	5187.3
29	0.320	0.039	0.5518	5306.3
30	0.320	0.063	0.5662	5532.3
31	0.535	0.003	0.4350	3866.7
32	0.523	0.007	0.4395	4164.1
33	0.514	0.016	0.4593	4164.1
34	0.540	0.030	0.4597	4247.4
35	0.532	0.057	0.4867	4342.6
36	0.522	0.090	0.4688	4461.6
37	0.530	0.175	0.4980	4937.5
38	0.533	0.309	0.5655	5710.8
39	0.802	0.003	0.3660	3271.8
40	0.802	0.006	0.3725	3271.8
41	0.798	0.010	0.3770	3569.3
42	0.787	0.022	0.4135	3985.7
43	0.790	0.047	0.4455	4223.6
44	0.778	0.104	0.4747	4699.5
45	0.786	0.196	0.4960	4997.0
46	0.789	0.369	0.5593	5532.3
47	0.196	0.002	0.6167	6686.4
48	0.414	0.002	0.5313	5532.3
49	0.450	0.003	0.5425	5353.9
50	0.315	0.003	0.5840	5770.3

Also given are the lengths, velocities and holdup values corresponding to the different zones of the slug units.

Taylor Bubble Translational Velocity. The rise velocity of a Taylor bubble in an annulus filled with a stagnant liquid column has been analyzed in Part I of this study. It was found that the Taylor bubble rise velocity can be predicted using the equiperipheral diameter concept. Thus, the translational velocity of the Taylor bubble is given by

$$V_T = 1.2(V_{SL} + V_{SG}) + 0.345\sqrt{g(D_C + D_T)} \qquad (17)$$

Mass Balance in Slug and Film Zones. Viewed from an external coordinate system, all slug variables change with respect to both time and space. However, for a coordinate system traveling at the translational velocity, slug variables are independent of time and vary only with respect to space. Thus, it is convenient to carry out the analysis in the translational velocity coordinate system. Also, assuming incompressible flow at a given location, the mass balance can be expressed in terms of volumetric flow rates.

A mass balance on the liquid phase between planes A-A and B-B of Fig. 9 yields

$$(V_T - V_{LLS})H_{LS} = (V_T + V_{LLF})H_{LF} \qquad (18)$$

where V_{LLS} is the in-situ liquid velocity in the liquid slug; V_{LLF} is the in-situ liquid velocity in the film surrounding the Taylor bubble, which is taken positive for downward flow; H_{LF} is the liquid holdup at a cross section that contains the terminal film thickness; and H_{LS} is the liquid holdup in the liquid slug.

Similarly, the mass balance for the gas phase yields

$$(V_T - V_{GLS})(1 - H_{LS}) = (V_T - V_{GTB})(1 - H_{LF}) \qquad (19)$$

where V_{GLS} and V_{GTB} are the in-situ gas velocities in the liquid slug and Taylor bubble, respectively.

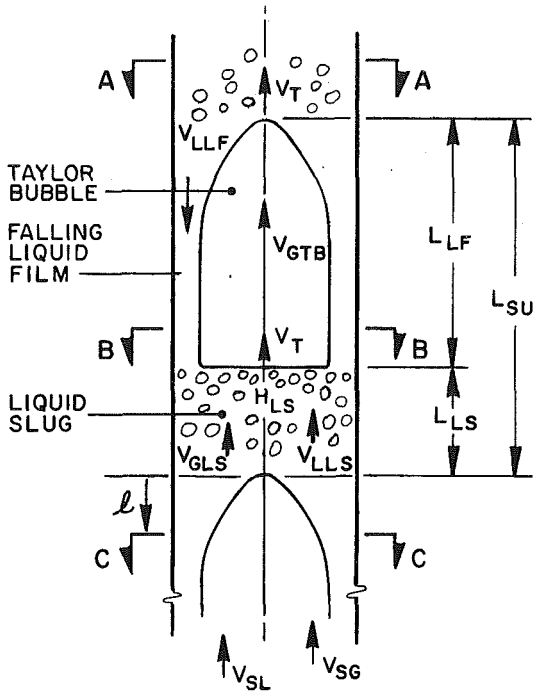

LEGEND

V_{SL}	SUPERFICIAL LIQUID VELOCITY
V_{SG}	SUPERFICIAL GAS VELOCITY
V_{LLS}	IN-SITU LIQUID VELOCITY IN THE LIQUID SLUG
V_{GLS}	IN-SITU GAS VELOCITY IN THE LIQUID SLUG
V_{LLF}	IN-SITU LIQUID VELOCITY IN THE LIQUID FILM
V_{GTB}	IN-SITU GAS VELOCITY IN THE TAYLOR BUBBLE
V_T	TAYLOR BUBBLE TRANSLATIONAL VELOCITY
H_{LS}	LIQUID HOLDUP IN THE LIQUID SLUG
L_{LS}	LENGTH OF THE LIQUID SLUG
L_{LF}	LENGTH OF THE LIQUID FILM
L_{SU}	LENGTH OF THE SLUG UNIT

Fig. 9 Idealized slug unit—geometry and parameters

Liquid Slug Zone. The liquid and gas phases in the liquid slug zone are assumed to behave analogous to fully developed bubble flow conditions. Following Barnea and Brauner (1985), it is proposed that the liquid holdup in the slug zone can be determined from the liquid holdup occurring at the transition boundary between bubble and slug flow. In the present study the liquid holdup at the bubble-slug transition boundary is constant. Therefore, the holdup in the liquid slug is also constant and has the same value as at the transition conditions.

Using the experimental results for the concentric annulus, the liquid holdup in the liquid slug zone is $H_{LS}=0.80$. Similarly, for the fully eccentric annulus, $H_{LS}=0.85$.

Slippage takes place in the liquid slug zone as the bubbles rise through the liquid phase. The slip velocities can be approximated by the bubble rise velocity in bubble swarm as previously given in Eq. (2); namely

$$V_S=V_{GLS}-V_{LLS}=1.53\left[\frac{(\rho_L-\rho_G)g\sigma}{\rho_L^2}\right]^{1/4}(H_{LS})^{1/2} \quad (20)$$

The bubble swarm index value of 0.5, determined experimentally and used throughout this study, agrees with the value used by Fernandes et al. (1983).

Since the total volumetric flow rate is constant at any section, a mass balance for the liquid slug region yields

$$(V_{SL}+V_{SG})A=V_{LLS}H_{LS}A+V_{GLS}(1-H_{LS})A \quad (21)$$

where the configuration flow area is

$$A=\frac{\pi}{4}(D_C^2-D_T^2) \quad (22)$$

Combining Eqs. (20) and (21), the in-situ liquid velocity in the liquid slug zone becomes

$$V_{LLS}=(V_{SL}+V_{SG})-1.53\left[\frac{(\rho_L-\rho_G)g\sigma}{\rho_L^2}\right]^{1/4}(H_{LS})^{1/2}(1-H_{LS}) \quad (23)$$

Similarly, the gas phase velocity in the liquid slug, V_{GLS}, can be determined from Eqs. (20) and (23).

Overall Mass Balances. The flow of gas and liquid along a slug unit was assumed previously to be incompressible. Thus, mass and volume balances are equivalent. An overall volume balance on the liquid phase yields

$$V_{SL}=V_{LLS}H_{LS}\frac{L_{LS}}{L_{SU}}-V_{LLF}H_{LF}\frac{L_{LF}}{L_{SU}} \quad (24)$$

where the slug unit length, L_{SU}, is

$$L_{SU}=L_{LF}+L_{LS} \quad (25)$$

Combining Eqs. (24) and (25) yields

$$\frac{L_{LS}}{L_{SU}}=\frac{V_{SL}+V_{LLF}H_{LF}}{V_{LLS}H_{LS}+V_{LLF}H_{LF}} \quad (26)$$

A similar procedure can be applied for the gas phase. Since gas flow rates in the liquid slug and in the Taylor bubble are both flowing upward, this yields

$$\frac{L_{LS}}{L_{SU}}=\frac{V_{SG}-(1-H_{LF})V_{GTB}}{(1-H_{LS})V_{GLS}-(1-H_{LF})V_{GTB}} \quad (27)$$

Liquid Film Zone—Developed Taylor Bubble. Comparison between the gas and liquid phases allows the assumption that the Taylor bubble is a region of approximately constant pressure. Also, neglecting interfacial shear stress, the liquid film flowing downward and surrounding the Taylor bubble can be considered as a free falling film.

The free falling film is assumed to have a thickness and flow rate relationship, at the bottom of the Taylor bubble, identical to that for a falling film on the surface of a vertical plane or cylinder. This situation is expected to be valid when the entry region for developing the velocity profile is less than the length of the film. The relationship between the film thickness and the film velocity for this case is given by

$$V_{LLF}=\left\{\frac{\delta^{1-C_M}}{C_K\left[\frac{\mu_L^2}{g(\rho_L-\rho_G)\rho_L}\right]^{1/3}}\right\}^{1/C_M}\frac{1}{\left(\frac{4\rho_L}{\mu_L}\right)} \quad (28)$$

The indices C_K and C_M depend on the velocity regime in the film zone. The Reynolds number associated with the liquid film flow is

$$\mathrm{Re}_{LF}=\frac{4\rho_L V_{LLF}\delta}{\mu_L} \quad (29)$$

For laminar flow, $\mathrm{Re}_{LF}<1000$, the indices C_K and C_M were analytically determined to be 0.9086 and 1/3, respectively, (Wallis, 1969). For turbulent flow, $\mathrm{Re}_{LF}>1000$, Fernandes et al. (1983) recommended using $C_K=0.0682$ and $C_M=2/3$. These values were experimentally determined by Brotz (Fernandes et al., 1983).

For the case where the bubble cap region is negligible, and the film reaches a terminal constant thickness, the liquid holdup in the film zone can be determined from the flow geometry and the film thickness δ

$$H_{LF}=\frac{4D_C}{(D_C+D_T)}\left(\frac{\delta}{(D_C-D_T)}\right)-\frac{4(D_C-D_T)}{(D_C+D_T)}\left(\frac{\delta}{D_C-D_T}\right)^2 \quad (30)$$

Film Zone—Developing Taylor Bubble. In the previous film zone treatment, the film length was assumed to be sufficiently long for the existing curvature of the Taylor bubble in the cap region to have a negligible influence on the results. However, substantial error can be introduced if the Taylor bubble consists only of a cap bubble. The film thickness then varies continuously along the film zone rather than reaching a constant terminal value. The error introduced is minor in the liquid holdup calculation, but can be significant for pressure gradient calculations.

The objective of this section is two fold: to determine if the developed Taylor bubble with a terminal film thickness assumption is fulfilled; and, if not, to determine the holdup and velocity profiles for a developing bubble.

The Taylor bubble cap length, L_C, is measured from the nose of the bubble to the point where the thickness in the surrounding liquid film reaches the so-called Nusselt thickness value, δ_N. This thickness is the one expected for a free falling film under laminar flow, and can be predicted analytically as

$$\delta_N = \left[\frac{3\,Q_{LLF}\mu_L}{\pi D_C g(\rho_L - \rho_G)}\right]^{1/3} \tag{31}$$

where Q_{LLF} is the downward volumetric flow rate of liquid.

As mentioned by Nicklin et al. (1962), the viscous forces at the top region of the Taylor bubble are negligible. The application of Bernoulli's theorem in this region gives the velocity of the liquid film relative to the nose of the bubble to be

$$V_{LLF}^R = V_{LLF} + V_T = (2gl)^{1/2} \tag{32}$$

where l is the distance from the nose of the bubble to the point of interest. The net volumetric flow rate across the plane C-C in Fig. 9 is

$$(V_{SL} + V_{SG})A = V_{GTB}A_{TB} - (A - A_{TB})V_{LLF} \tag{33}$$

Equation (33) can be rewritten in terms of volumetric flow rates as

$$Q_L + Q_G = Q_{GTB} - Q_{LLF} \tag{34}$$

where Q_L, Q_G, and Q_{GTB} are the total liquid flow rate, the total gas flow rate, and gas flow rate in the Taylor bubble, respectively.

Using Eq. (19), Eq. (34) can be written as

$$Q_{LLF} = [V_T A_{TB} - (V_T - V_{GLS})(1 - H_{LS})A] - (Q_L + Q_G) \tag{35}$$

When the liquid film reaches the Nusselt film thickness δ_N value, the resulting Taylor bubble area A_{TB} in an annulus is

$$A_{TB}^N = \frac{\pi}{4}[(D_C - 2\delta_N)^2 - D_T^2] \tag{36}$$

Using Eqs. (22), (31), (35), and (36), through an iterative procedure the Nusselt film thickness, δ_N, can be determined. Designating L_C as the length of the Taylor cap bubble in which the liquid film reaches the Nusselt thickness value, and combining Eqs. (22) and (33) and (36), for $l = L_C$, one can obtain

$$L_C = \frac{1}{2g}\left[V_T + \frac{V_{GTB}A_{TB}^N}{(A - A_{TB}^N)} - \left(\frac{Q_G + Q_L}{A - A_{TB}^N}\right)\right]^2 \tag{37}$$

where V_{GTB} is determined for the section in which δ_N exists.

Comparison can now be made between the cap length L_C and the length of the film zone calculated for the developed bubble, L_{LF}. The developed film length L_{LF} can be determined from Eq. (25) and either Eq. (26) or (27), for a given value of liquid slug length, L_{LS}. Liquid slug length in upward vertical fully developed slug flow in pipes can be dependent on the gas and liquid flow rates. However, various investigators (Fernandes et al., 1983; and Taitel et al., 1980) have showed that over a wide range of flow conditions, the slug length has a fairly constant value. Taitel et al. (1980) suggested a liquid slug length value of 16 pipe diameters for establishing stable slugs. Hence, for annuli, it is assumed that

$$L_{LS} = 16\,D_H = 16(D_C - D_T) \tag{38}$$

Comparison can now be made between L_C and L_{LF}. If $L_{LF} > L_C$, the assumption of a developed bubble is fulfilled and the average liquid holdup in the film zone can be determined from Eq. (30). For the case of a developing bubble region, $L_C > L_{LF}$, the film profile should be taken into consideration as follows.

The volume of gas in the Taylor bubble can be evaluated through the integral

$$\forall_{GTB} = \int_0^{L_{LF}^*} A_{TB}\,dl \tag{39}$$

where L_{LF}^* is the true existing liquid film length.

An overall volume balance for the gas phase yields

$$\forall_{GSU} = \forall_{GTB} + \forall_{GLS} \tag{40}$$

where $\forall_{GSU}$ and $\forall_{GLS}$ are the volumes of gas in the entire slug unit and in the liquid slug, respectively. Accounting for the time of passage of a slug unit, Eq. (40) can be rewritten as

$$\forall_{GTB} = \frac{V_{SG}}{V_T}AL_{LF}^* + \left[\frac{V_{SG} - V_{GLS}(1 - H_{LS})}{V_T}\right]AL_{LS} \tag{41}$$

Combining Eqs. (39) and (41), yields

$$\frac{V_{SG}}{V_T}L_{LF}^* + \left[\frac{V_{SG} - V_{GLS}(1 - H_{LS})}{V_T}\right]L_{LS} = \int_0^{L_{LF}^*}[1 - h_{LF}(l)]dl \tag{42}$$

where h_{LF} is the local liquid film holdup.

Combining Eqs. (18) and (32) yields

$$h_{LF}(l) = \frac{(V_T - V_{LLS})H_{LS}}{\sqrt{2gl}} \tag{43}$$

Substituting Eq. (43) into Eq. (42) and performing the integration results in

$$L_{LF}^{*2} + BL_{LF}^* + C = 0 \tag{44}$$

where

$$B = \left\{\frac{-2\left(1 - \frac{V_{SG}}{V_T}\right)\left[\frac{V_{SG} - V_{GLS}(1 - H_{LS})}{V_T}\right]L_{LS} + \left(\frac{2}{g}\right)(V_T - V_{LLS})^2 H_{LS}^2}{\left(1 - \frac{V_{SG}}{V_T}\right)^2}\right\} \tag{45}$$

and

$$C = \left\{\frac{\frac{V_{SG} - V_{GLS}(1 - H_{LS})}{V_T}L_{LS}}{\left(1 - \frac{V_{SG}}{V_T}\right)}\right\}^2 \tag{46}$$

The actual film length, L_{LF}^*, can now be determined from the solution of Eq. (44). Once this length is determined, the local liquid film velocity in this location can be determined from Eq. (32) as

$$V_{LLF} = V_{LLF}^R - V_T = \sqrt{2g\,L_{LF}^*} - V_T \tag{47}$$

Using Eq. (43), the average liquid film holdup for the entire film length can be determined as

$$H_{LF}=\frac{1}{L_{LF}^{*}}\int_{0}^{L_{LF}^{*}}\frac{(V_T-V_{LLS})H_{LS}}{\sqrt{2gl}}dl$$

or

$$H_{LF}=\frac{2(V_T-V_{LLS})H_{LS}}{\sqrt{2gL_{LF}^{*}}} \tag{48}$$

Average Liquid Holdup. The slug unit average liquid holdup, H_{SU}, can be determined as

$$H_{SU}=\left(\frac{L_{LS}}{L_{SU}}\right)H_{LS}+\left(1-\frac{L_{LS}}{L_{SU}}\right)H_{LF} \tag{49}$$

where L_{LS}/L_{SU} is determined from Eq. (26) and H_{LF} can be determined from Eq. (30) for a developed bubble. An iterative procedure on the film thickness δ is required. For the case of a developing bubble the average liquid holdup in the film, H_{LF}, is calculated from Eq. (48).

Pressure Gradients. Since the Taylor bubble is assumed to be a constant pressure region, the pressure drop occurring in the Taylor bubble and film zone is neglected. Thus, all the pressure drop for an entire slug unit is assumed to occur in the liquid slug zone. The pressure gradient terms are thus determined for the liquid slug zone, and then averaged over the entire slug unit length.

The gravitation pressure gradient component for the slug unit is calculated through the slip density as

$$\left(\frac{dp}{dz}\right)_G=\rho_S g\frac{L_{LS}}{L_{SU}} \tag{50}$$

where the slip density for the gas-liquid mixture in the liquid slug is

$$\rho_S=\rho_L H_{LS}+\rho_G(1-H_{LS}) \tag{51}$$

The acceleration pressure gradient component is related to the amount of energy that is required to accelerate the liquid film flow rate, which is initially flowing downward, to the existing upward in-situ liquid velocity in the liquid slug.

$$\left(\frac{dp}{dz}\right)_A=\rho_L\frac{H_{LF}}{L_{SU}}(V_{LLF}+V_T)(V_{LLF}+V_{LLS}) \tag{52}$$

For the case of a developed Taylor bubble, H_{LF} and V_{LLF} are the average liquid holdup and film velocity in the entire film zone, respectively. For the case of a developing bubble, the terminal values for these parameters are used.

The friction pressure gradient is evaluated through the slip density given in Eq. (51), and the mixture velocity, i.e.,

$$\left(\frac{dp}{dz}\right)_F=\frac{2f}{D_H}\rho_S(V_{SG}+V_{SL})^2\frac{L_{LS}}{L_{SU}} \tag{53}$$

Determination of the Fanning friction factor is through the method presented in Part I of this study. The corresponding Reynolds number for the slug body is determined by Eq. (11), where ρ_S is the slug body slip density given by Eq. (51).

The total pressure gradient for the slug flow pattern can now be expressed by combining Eqs. (50), (52), and (53) to obtain

$$\left(\frac{dp}{dz}\right)_T=\left[\rho_S g L_{LS}+\rho_L H_{LF}(V_{LLF}+V_T)(V_{LLF}+V_{LLS})+\frac{2f}{D_H}\rho_S(V_{SG}+V_{SL})^2 L_{LS}\right]\frac{1}{L_{SU}} \tag{54}$$

Evaluation of Slug Flow Model. The model for slug flow was used to predict the liquid holdup and total pressure gradient for the tests given in Tables 5 and 6. The performance of the model can be evaluated by comparing predicted and measured results.

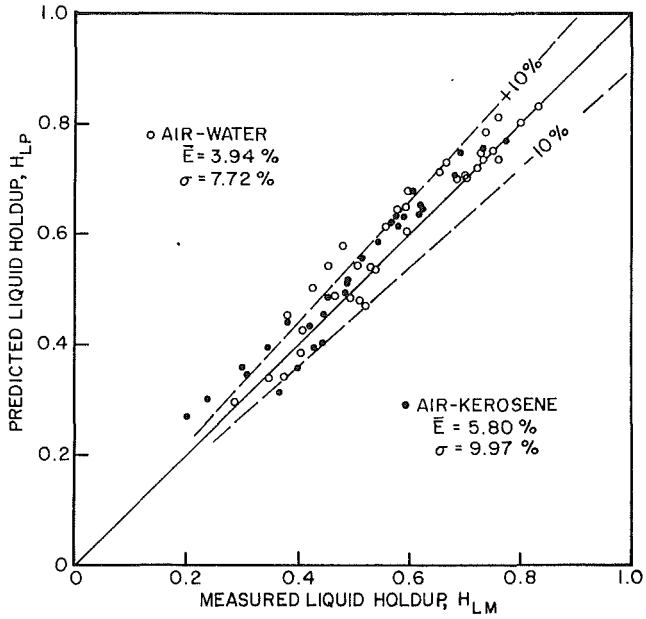

Fig. 10 Slug flow model performance—average volumetric liquid holdup in concentric annulus

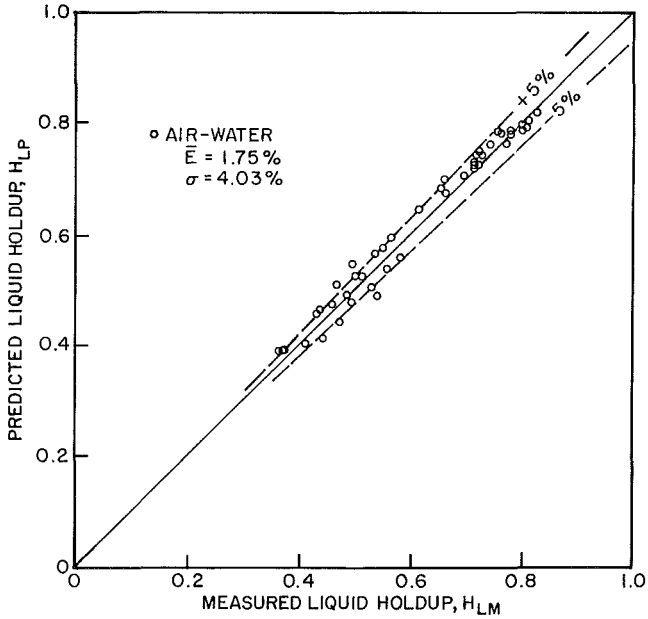

Fig. 11 Slug flow model performance—average volumetric liquid holdup in fully eccentric annulus

Figures 10 and 11 show the model performance for the average volumetric liquid holdup prediction in the concentric and fully eccentric annuli, respectively. The performance obtained by the model is good, with a slight overprediction of both air-kerosene and air-water mixtures. The standard deviations ranged from 4 to 10 percent, confirming reasonable scatter about the mean. The model performs slightly better for the air-water mixture.

Figures 12 and 13 show the model performance for the total pressure gradient prediction in the concentric and fully eccentric annulus, respectively. The agreement between the model and experimental results is good. As in the liquid holdup prediction, again the model performs slightly better for the air-water mixture. No significant differences are found in model

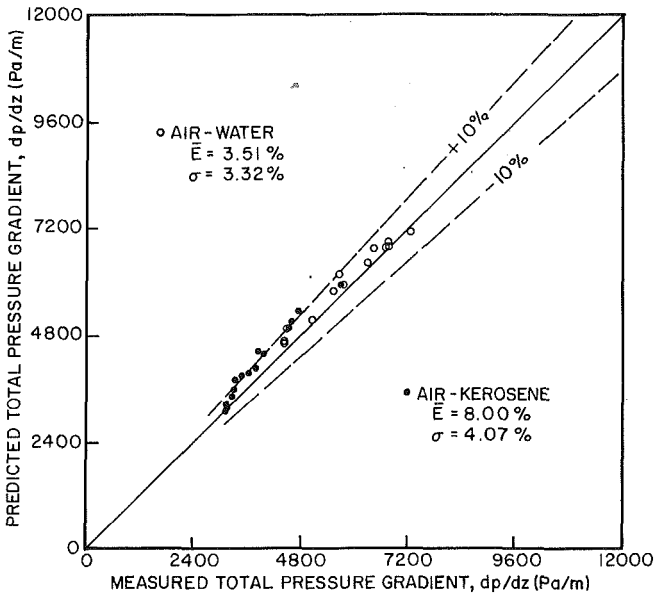

Fig. 12 Slug flow model performance—total pressure gradient in concentric annulus

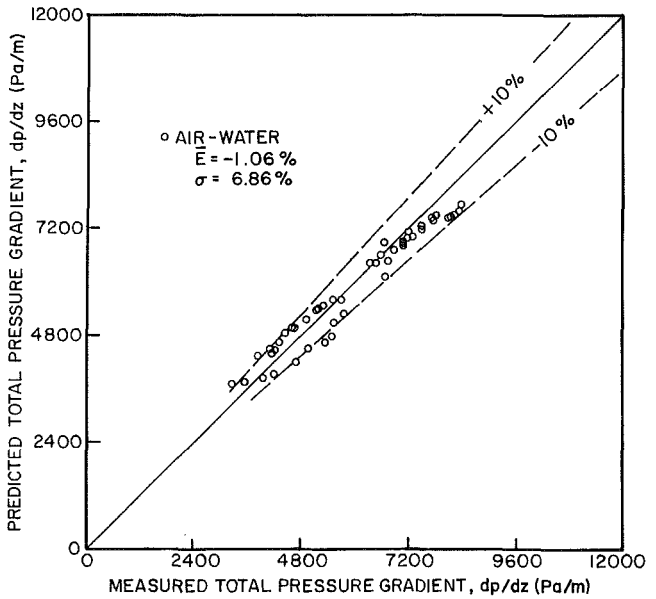

Fig. 13 Slug flow model performance—total pressure gradient in fully eccentric annulus

performance for the two annuli, suggesting that the model adequately accounts for eccentricity.

The slight overprediction of both the average liquid holdup and pressure gradient might result from treating the liquid holdup in the liquid slug as a constant. However, this value might decrease with an increase in the gas flow rate. Taking into consideration this variation might improve the performance of the model.

Annular Flow

Annular flow occurs at high superficial gas velocities and is characterized by a continuous fast moving gas phase flowing in the core of the annulus cross-sectional area. The liquid phase flows both as liquid films wetting the boundary walls and as tiny droplets entrained in the gas core. The outside film, wetting the casing inner wall, is usually thicker than the inner film flowing on the tubing outside wall. The gas and liquid droplets flowing in the core can be assumed as a homogeneous mixture due to the high velocity of the gas phase.

Table 7 Experimental liquid holdup and total pressure gradient in annular flow—concentric annulus

Test Number	Superficial Gas Velocity (m/s)	Superficial Liquid Velocity (m/s)	Liquid Holdup	Total Pressure Gradient (Pa/m)
air-water				
1	13.085	0.050	0.0900	--------
2	12.806	0.111	0.1120	--------
3	11.669	0.501	0.1773	--------
4	15.803	0.499	0.1175	--------
5	20.660	0.098	0.0500	--------
6	16.830	0.494	0.1290	--------
7	22.067	0.044	0.0300	1470.0
8	21.893	0.111	0.0510	2038.4
9	16.610	0.523	0.1185	4671.7
10	21.256	0.111	0.0530	2125.7
11	16.680	0.548	0.1250	5115.8
12	13.023	0.299	0.1315	3176.6
air-kerosene				
13	7.883	0.104	0.1165	--------
14	7.938	0.199	0.1385	--------
15	7.061	0.102	0.1240	--------
16	11.164	0.199	0.1065	--------
17	10.954	0.299	0.1260	--------
18	21.503	0.100	0.0300	1467.3
19	21.320	0.199	0.0530	1836.1
20	18.991	0.399	0.1000	3331.2
21	16.938	0.598	0.1265	4164.1
22	12.547	0.056	0.0520	872.5
23	12.334	0.112	0.0735	1205.6
24	11.981	0.199	--------	1578.4
25	11.545	0.399	--------	2696.7

Table 8 Experimental liquid holdup and total pressure gradient in annular flow—fully eccentric annulus

Test Number	Superficial Gas Velocity (m/s)	Superficial Liquid Velocity (m/s)	Liquid Holdup	Total Pressure Gradient (Pa/m)
air-water				
1	10.258	0.227	0.1515	2641.2
2	17.891	0.259	0.0955	3176.6
3	18.043	0.334	0.1050	3747.7
4	19.947	0.105	0.0535	1939.3
5	16.180	0.104	0.0770	1689.4
6	20.743	0.088	0.0465	1844.1
7	21.201	0.051	0.0356	1499.1
8	17.166	0.051	0.0500	1249.2
9	16.900	0.080	0.0603	1558.6
10	17.000	0.104	0.0690	1796.5
11	12.458	0.045	0.0735	1118.4
12	16.184	0.518	0.1250	4878.0
13	17.937	0.346	0.1080	3747.7

Experimental Holdup and Pressure Gradient Data. The experimental data collected for the average volumetric liquid holdup and the total pressure gradient are given in Tables 7 and 8 along with the corresponding superficial phase velocities. Table 7 shows the data acquired for air-water and air-kerosene in the concentric annulus. Similarly, Table 8 shows the data acquired for air-water in the fully eccentric annulus. As can be seen in Table 7, not all the tests include data for both liquid holdup and pressure gradient. The data show low liquid holdup values, sometimes less than 3 percent, and low pressure gradient values. This flow pattern exhibits the lowest values of liquid holdup and pressure gradient along all possible flow patterns in upward vertical flow.

Annular Flow Model. Figure 14 shows a schematic description of annular flow in a concentric annulus. The model is based on equilibrium fully developed flow. The phases are assumed to be incompressible. The liquid films are assumed to have uniform thickness, but with different values. The gas and liquid droplets flowing in the annulus core are assumed to flow as a homogeneous mixture with the same velocity.

Linear Momentum Equations. The conservation of linear momentum for the outer (casing) liquid film yields

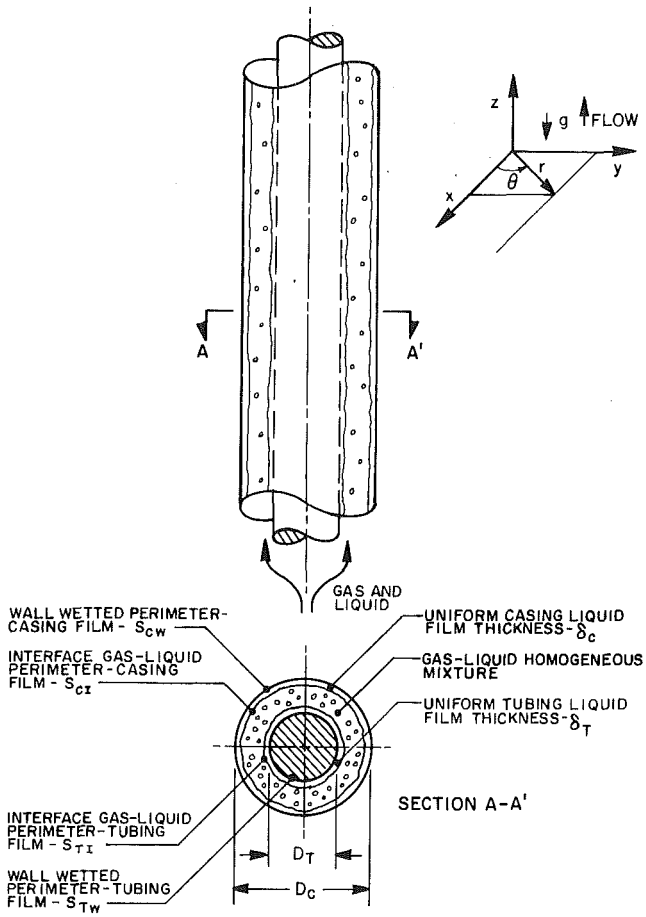

Fig. 14 Idealized annular flow—geometry and parameters

$$\left(\frac{dp}{dz}\right)_{CL} + \tau_{CW}\frac{S_{CW}}{A_{CL}} - \tau_{CI}\frac{S_{CI}}{A_{CL}} + \rho_L g = 0 \tag{55}$$

In this equation, $(dp/dz)_{CL}$ is the total pressure gradient for the casing liquid film, τ_{CW} and τ_{CI} are the shear stresses occurring at the casing wall and liquid film-core mixture interface, respectively. S_{CW} and S_{CI} are the wetted liquid perimeters on the casing wall and liquid film-core mixture interface, respectively. A_{CL} is the total area of the casing liquid film.

Similarly, a linear momentum balance for the inner (tubing) film yields

$$\left(\frac{dp}{dz}\right)_{TL} + \tau_{TW}\frac{S_{TW}}{A_{TL}} - \tau_{TI}\frac{S_{TI}}{A_{TL}} + \rho_L g = 0 \tag{56}$$

where all the terms have the same meaning as given for similar terms in Eq. (55).

A linear momentum balance for the gas-droplets mixture flowing the core of the annulus configuration yields

$$\left(\frac{dp}{dz}\right)_{\text{core}} + \tau_{CI}\frac{\delta_{CI}}{A_{\text{core}}} + \tau_{TI}\frac{S_{TI}}{A_{\text{core}}} + \rho_{\text{core}} g = 0 \tag{57}$$

where $(dp/dz)_{\text{core}}$ is the total pressure gradient for the mixture in the core, ρ_{core} is the density of the mixture in the core, and A_{core} is the area of the core occupied by the mixture.

The gas liquid interfaces are considered stable; hence, the following equilibrium condition exists:

$$\left(\frac{dp}{dz}\right)_{CL} = \left(\frac{dp}{dz}\right)_{TL} = \left(\frac{dp}{dz}\right)_{\text{core}} \tag{58}$$

Using the equilibrium condition and the linear momentum equations given by Eqs. (55)–(57), two combined momentum equations are written as follows:

$$-\tau_{CW}\frac{S_{CW}}{A_{CL}} + \tau_{CI}\frac{S_{CI}}{A_{CL}} + \tau_{CI}\frac{S_{CI}}{A_{\text{core}}} + \tau_{TI}\frac{S_{TI}}{A_{\text{core}}} - (\rho_L - \rho_{\text{core}})g = 0 \tag{59}$$

and

$$-\tau_{TW}\frac{S_{TW}}{A_{TL}} + \tau_{TI}\frac{S_{TI}}{A_{TL}} + \tau_{CI}\frac{S_{CI}}{A_{\text{core}}} + \tau_{TI}\frac{S_{TI}}{A_{\text{core}}} - (\rho_L - \rho_{\text{core}})g = 0 \tag{60}$$

Based on the annulus geometry given in Fig. 14, and since the films are considered uniform in thickness, geometrical relationships for the relevant dimensions can be written. The casing liquid film area, the tubing liquid film area and the core area for the mixture are given, respectively, by

$$\left.\begin{aligned} A_{CL} &= \pi\delta_C(D_C - \delta_C) \\ A_{TL} &= \pi\delta_T(D_T + \delta_T) \\ A_{\text{core}} &= \frac{\pi}{4}[D_C^2 - D_T^2 - 4\delta_C(D_C - \delta_C) - 4\delta_T(D_T + \delta_T)] \end{aligned}\right\} \tag{61}$$

where δ_C and δ_T are the casing liquid film thickness and tubing liquid film thickness, respectively.

The perimeters associated with the casing liquid film and tubing liquid film, for both the wall and interface sides, are given by

$$\left.\begin{aligned} S_{CW} &= \pi D_C \\ S_{CI} &= \pi(D_C - 2\delta_C) \\ S_{TW} &= \pi D_T \\ S_{TI} &= \pi(D_T + 2\delta_T) \end{aligned}\right\} \tag{62}$$

Applying the hydraulic diameter concept to the casing liquid film, tubing liquid film and core, and using the set of equations given by Eqs. (61) and (62), the hydraulic diameters associated with each of the regions mentioned can be written as

$$\left.\begin{aligned} D_{CL} &= 4\delta_C\left(1 - \frac{\delta_C}{D_C}\right) \\ D_{TL} &= 4\delta_T\left(1 + \frac{\delta_T}{D_T}\right) \\ D_{\text{core}} &= \frac{[D_C^2 - D_T^2 - 4\delta_C(D_C - \delta_C) - 4\delta_T(D_T + \delta_T)]}{(D_C - 2\delta_C) + (D_T + 2\delta_T)} \end{aligned}\right\} \tag{63}$$

The wall shear stress is given by

$$\tau_w = f_w \rho \frac{V^2}{2} \tag{64}$$

where τ_w is the respective wall shear stress, ρ is the density for the phase which wets the wall, V is the in-situ average phase velocity, and f_w is the associated Fanning friction factor. This Fanning friction factor is evaluated by a Blasius-type expression as given by

$$f_w = C\text{Re}^{-x} \tag{65}$$

where $x = 1$ for laminar flow and $x = 0.25$ for turbulent flow. The coefficient C is evaluated by taking into account the configuration geometry as described in Part I of the study.

Neglecting the liquid film velocities in comparison with the core velocity, the interfacial shear stress is approximated by

$$\tau_I = f_I \rho_{\text{core}} \frac{V_{\text{core}}^2}{2} \tag{66}$$

where τ_I is the interface shear stress, V_{core} is the in-situ velocity in the core, and f_I is the Fanning friction factor associated

with the interface. For vertical annular flow through pipes, Wallis (1969) suggested that

$$f_I = C\left(1 + 300\frac{\delta}{D}\right) \tag{67}$$

where C is a constant, δ is the liquid film thickness, and D is the pipe diameter. Modifying for annuli, the casing film-interface and tubing film-interface friction factors are given, respectively, by

$$f_I = (f_{\text{core}})_S\left(1 + 300\frac{\delta_C}{D_C}\right) \tag{68}$$

and

$$f_I = (f_{\text{core}})_S\left(1 + 300\frac{\delta_T}{D_T}\right) \tag{69}$$

where $(f_{\text{core}})_S$ is the friction factor corresponding to the superficial velocity existing in the core.

Using the shear stress and the geometrical relationship defined in Eqs. (61)-(69), the combined linear momentum for the casing liquid film and mixture in the core, given by Eq. (59), can be rewritten as

$$-f_{CW}\rho_L\frac{V_{CL}^2}{2}\frac{D_C}{\delta_C(D_C-\delta_C)} + (f_{\text{core}})_S\left(1+300\frac{\delta_C}{D_C}\right)\rho_{\text{core}}\frac{V_{\text{core}}^2}{2}\frac{(D_C-2\delta_C)}{\delta_C(D_C-\delta_C)}$$
$$+ (f_{\text{core}})_S\left(1+300\frac{\delta_C}{D_C}\right)\rho_{\text{core}}\frac{V_{\text{core}}^2}{2}\frac{4(D_C-2\delta_C)}{[D_C^2-D_T^2-4\delta_C(D_C-\delta_C)-4\delta_T(D_T+\delta_T)]}$$
$$+ (f_{\text{core}})_S\left(1+300\frac{\delta_T}{D_T}\right)\rho_{\text{core}}\frac{V_{\text{core}}^2}{2}\frac{4(D_T+2\delta_T)}{[D_C^2-D_T^2-4\delta_C(D_C-\delta_C)-4\delta_T(D_T+\delta_T)]} - (\rho_L-\rho_{\text{core}})g = 0 \tag{70}$$

Similarly, the combined linear momentum relationship for the tubing liquid film and mixture in the core, as given by Eq. (60), can be rewritten as

$$-f_{TW}\rho_L\frac{V_{TL}^2}{2}\frac{D_T}{\delta_T(D_T+\delta_T)} + (f_{\text{core}})_S\left(1+300\frac{\delta_T}{D_T}\right)\rho_{\text{core}}\frac{V_{\text{core}}^2}{2}\frac{(D_T+2\delta_T)}{\delta_T(D_T+\delta_T)}$$
$$+ (f_{\text{core}})_S\left(1+300\frac{\delta_C}{D_C}\right)\rho_{\text{core}}\frac{V_{\text{core}}^2}{2}\frac{4(D_C-2\delta_C)}{[D_C^2-D_T^2-4\delta_C(D_C-\delta_C)-4\delta_T(D_T+\delta_T)]}$$
$$+ (f_{\text{core}})_S\left(1+300\frac{\delta_T}{D_T}\right)\rho_{\text{core}}\frac{V_{\text{core}}^2}{2}\frac{4(D_T+2\delta_T)}{[D_C^2-D_T^2-4\delta_C(D_C-\delta_C)-4\delta_T(D_T+\delta_T)]} - (\rho_L-\rho_{\text{core}})g = 0 \tag{71}$$

Phase Continuity Equations. The continuity for the liquid phase, which flows in the form of two films wetting the bounding walls and as droplets entrained in the gas core, yields

$$V_{SL} = V_{TL}H_{TL} + V_{CL}H_{CL} + V_{SL}Fe \tag{72}$$

where H_{TL} is the in-situ liquid holdup in the tubing film, H_{CL} in the in-situ liquid holdup in the casing film, and Fe is the fraction of liquid entrained in the gas core.

The continuity for the gas phase, which flow in the core bounded by the two liquid films, yields

$$V_{SG} = V_{\text{core}}(1 - H_{L,\text{TOTAL}}) \tag{73}$$

where V_{core} is in the in-situ gas velocity in the core and $H_{L,\text{TOTAL}}$ is the total in-situ liquid holdup in the annulus.

The liquid holdup for the casing liquid film is the ratio between the area for this film and the total annulus area. Using Eqs. (61) and (22) yields

$$H_{CL} = \frac{\pi\delta_C(D_C-\delta_C)}{\frac{\pi}{4}(D_C^2-D_T^2)}$$

and

$$H_{CL} = \frac{4\delta_C}{D_C}\frac{(1-\delta_C/D_C)}{(1-K^2)} \tag{74}$$

where K is the annulus pipe diameter ratio, D_T/D_C.

Similarly, the in-situ liquid holdup for the tubing liquid film is given by

$$H_{TL} = \frac{4\delta_T}{D_C}K\frac{(1+\delta_T/D_T)}{(1-K^2)} \tag{75}$$

The in-situ liquid holdup in the core, where the gas-liquid mixture is assumed homogeneous, is given by

$$H_{L,\text{core}} = \frac{V_{SL}Fe}{V_{SL}Fe + V_{SG}} \tag{76}$$

The total liquid holdup in the annulus is the sum of the liquid holdup in the core and in the two films. Using Eqs. (22), (61), (74), (75), and (76) yields

$$H_{L,\text{TOTAL}} = \frac{4}{D_C(1-K^2)}[\delta_C(1-\delta_C/D_C) + \delta_T K(1+\delta_T/D_T) + \frac{V_{SL}Fe}{(V_{SL}Fe+V_{SG})(1-K^2)}\left[1-K^2-\frac{4\delta_C}{D_C}\left(1-\frac{\delta_C}{D_C}\right) - \frac{4\delta_T K}{D_C}(1+\delta_T/D_T)\right] \tag{77}$$

A correlation for predicting the liquid fraction entrained in the gas core of long pipes under annular two-phase flow was developed by Wallis (1969) as

$$Fe = 1 - \exp[-0.125(\phi - 1.5)] \tag{78}$$

where the gas dimensionless number, ϕ, is given by

$$\phi = 10^4 V_{SG}\frac{\mu_G}{\sigma}\left(\frac{\rho_G}{\rho_L}\right)^{1/2} \tag{79}$$

This correlation is reported to perform reasonably well for situations where the liquid does not occupy a considerable amount of the total cross-sectional area and the viscous forces in the liquid are considered negligible and is used throughout this study.

Tubing-Casing Liquid Film Thickness Ratio. As observed in this study and reported by previous investigators (Andersen and Wurtz, 1981), the casing liquid film is thicker than the tubing liquid film. A prediction for the ratio between the tubing film thickness and casing film thickness is developed by assuming equilibrium between the entrainment and deposition rates of liquid droplets. In this development it is also assumed that an isotropic scattering mechanism applies for the liquid droplets in the core. The droplets can travel in any direction in the core, remaining entrained or depositing in one of the two liquid films.

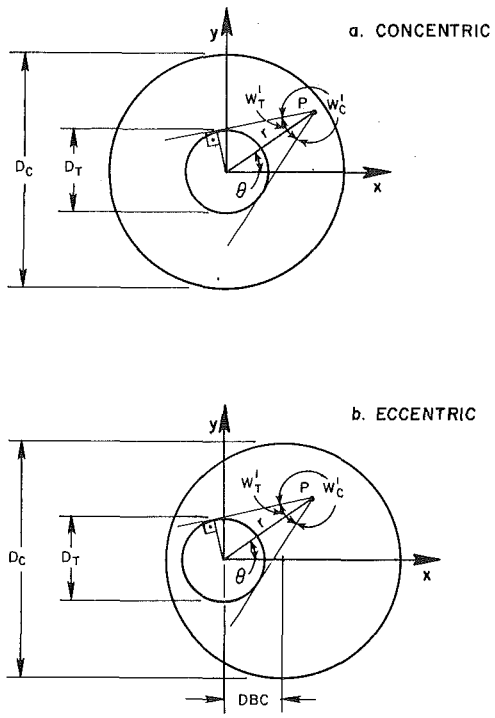

Fig. 15 Planar angles of view of annuli

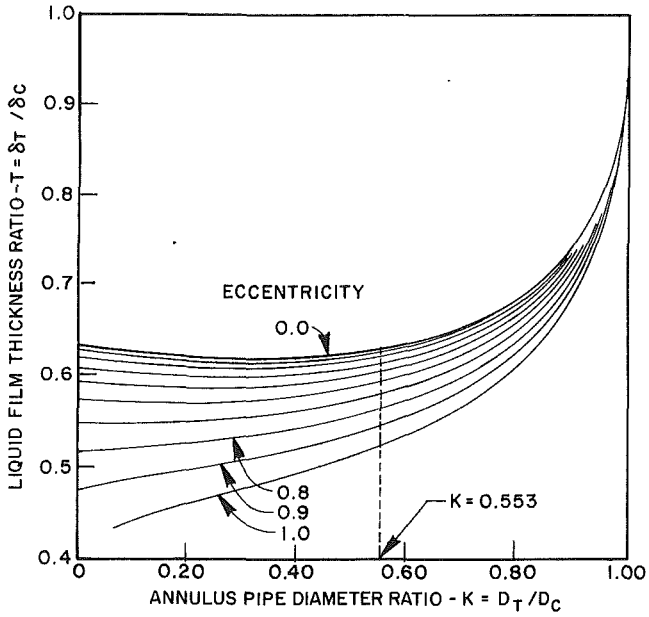

Fig. 16 Liquid film thickness ratio in annuli

The liquid droplets entrainment rate is assumed to be dependent on the film thickness, a mass transfer coefficient and liquid film projected area at the wall side. Thus, the entrainment rate associated with the casing liquid film is

$$E_{CL} = k_E \delta_C \pi D_C L \tag{80}$$

Similarly, the entrainment rate associated with the tubing liquid film is given by

$$E_{TL} = k_E \delta_T \pi D_T L \tag{81}$$

The liquid droplets deposition rate is assumed to be dependent on the liquid concentration in the gas core, a deposition mass transfer coefficient, and the solid angle W associated with the deposition area seen by the entrained liquid droplet. Thus, the deposition rate associated with the casing liquid film is given by

$$D_{CL} = k_D C_{\text{core}} W_C \tag{82}$$

Similarly, the deposition rate associated with the tubing liquid film is given by

$$D_{TL} = k_D C_{\text{core}} W_T \tag{83}$$

At equilibrium conditions, the liquid droplets deposition and entrainment rates are equal for each liquid film. A ratio involving these equalities yields

$$\frac{D_{TL}}{D_{CL}} = \frac{E_{TL}}{E_{CL}}$$

or, using Eqs. (80)–(83)

$$T = \frac{\delta_T}{\delta_C} = \frac{W_T}{W_C}\frac{1}{K} \tag{84}$$

where T is the ratio between the tubing and casing liquid film thicknesses and K is the annulus pipe diameter ratio.

When long pipes form the annulus, the film thickness ratio dependency on the solid angle can be assumed as dependent on the planar angles of view associated with the tubing and casing walls. As shown in Fig. 15, these planar angles, W_T' and W_C' sum up to 2π. Thus, the film thickness ratio given in Eq. (84) can be approximated to

$$T = \frac{\delta_T}{\delta_C} = \frac{W_T'}{(2\pi - W_T')K} \tag{85}$$

where

$$W_T' = 2\sin^{-1}\left(\frac{D_T}{2r}\right) \tag{86}$$

and r is the vector distance from the liquid droplet position in the core to the center of the tubing, which is also considered the annulus center.

However, the angle of view for a liquid droplet entrained in the core is a function of the droplet position in this core. Averaging the angle of view in terms of the core area, Eq. (85) can be rewritten as

$$T = \frac{\delta_T}{\delta_C} = \frac{\langle W_T' \rangle}{(2\pi - \langle W_T' \rangle)K} \tag{87}$$

where $\langle W_T' \rangle$ is the angle of view associated with the tubing wall, averaged over the entire annulus cross-sectional area.

Averaging the local values for W_T' given by Eq. (86) over the entire cross-sectional area for a concentric annulus yields

$$\langle W_T' \rangle = \frac{16}{(D_C^2 - D_T^2)} \int_{D_T/2}^{D_C/2} \sin^{-1}\left(\frac{D_T}{2r}\right) r\,dr$$

$$= \frac{1}{(1-K^2)}\left[2\sin^{-1}(K) + 2K\sqrt{1-K^2} - K^2\pi\right] \tag{88}$$

where K is the annulus pipe diameter ratio.

Similarly, in eccentric annuli the average value for the tubing angle of view, $\langle W_T' \rangle$, can be reduced to

$$\langle W_T' \rangle = \frac{1}{\pi(1-K^2)} \int_0^{\pi} \left[8a^2 \sin^{-1}\left(\frac{K}{2a}\right) + 2K\sqrt{4a^2 - K^2} - K^2\pi \right] d\theta \tag{89}$$

where the parameter a is given by

$$a = \frac{e}{2}(1-K)\cos\theta + \frac{1}{2}\sqrt{e^{+2}(1-K)^2(\cos^2\theta - 1) + 1} \tag{90}$$

and e is the configuration degree of eccentricity. Notice that when $e = 0$ (concentric annulus), the parameter a given by Eq.

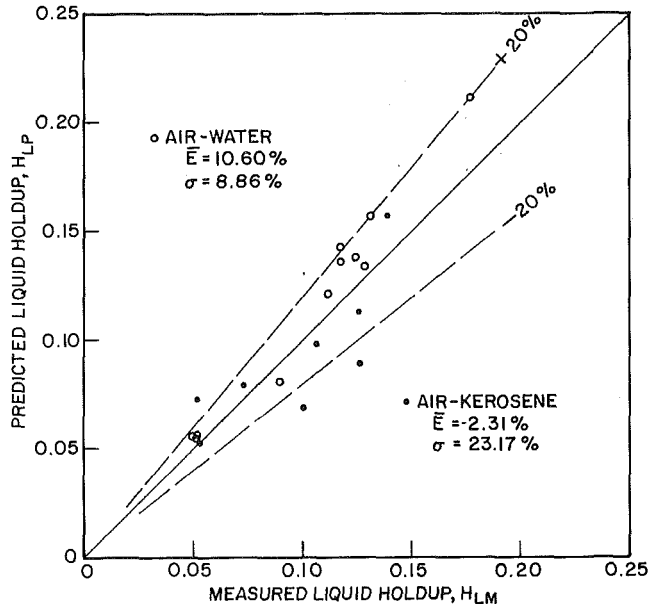

Fig. 17 Annular flow model performance—average volumetric liquid holdup in concentric annulus

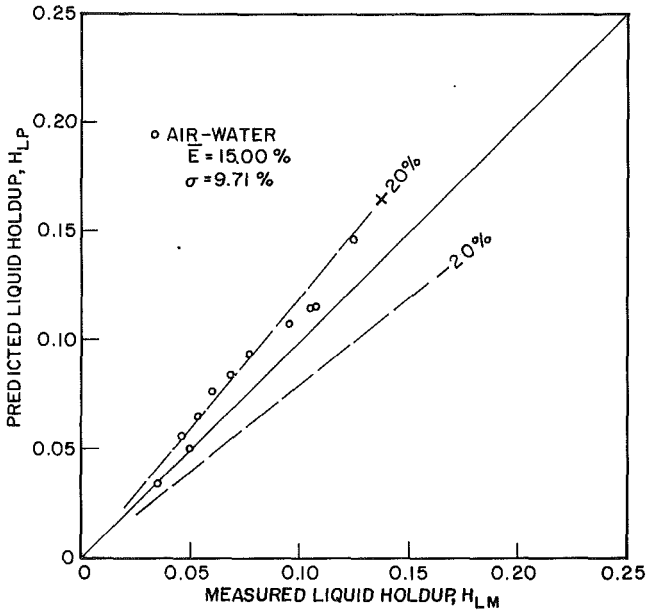

Fig. 18 Annular flow model performance—average volumetric liquid holdup in fully eccentric annulus

(90) reduces to 1/2. Consequently, the integrand expression in Eq. (89) becomes independent of the integration variable θ and the integral result is the one given previously by Eq. (88). However, if $e \neq 0$, no analytical solution was found for Eq. (89). The integration was carried out numerically by applying the Simpson's rule.

Figure 16 shows the results found for the tubing-casing liquid film thickness ratio, as given by Eq. (87), in terms of the annulus pipe diameter ratio and degree of eccentricity. During the numerical determination of the average angle of view for an eccentric annulus, singularities were found when the pipe diameter ratio was equal to zero. For a fully eccentric annulus, these singularities also appeared for extremely low pipe diameter ratio values. Consequently, the curves in Fig. 16 should not be used for liquid film ratio determination for an eccentric annulus in these singularity regions. The dashed vertical line in Fig. 16 also shows the predicted film thickness ratio for the annulus pipe diameter ratio used in this study.

Summary of Governing Equations—Dimensionless Form. The governing equations developed previously for the annular flow model can be presented in dimensionless form. The normalizing variable selected for length is the hydraulic diameter for the annulus configuration, given by

$$D_H = D_C - D_T \tag{10}$$

The normalizing variables selected for velocity are the superficial liquid velocity for the in-situ velocities in the liquid films and the core mixture velocity for the in-situ velocity in this region. This core velocity is given by

$$V_{M,\text{core}} = V_{SG} + Fe V_{SL} \tag{91}$$

where Fe is the liquid fraction entrained in the core.

Nondimensionalizing Eq. (70) yields

$$\tilde{V}_{CL}^{2-m} = \frac{\tilde{\delta}_C[1-\tilde{\delta}_C(1-K)]}{X_M^2 \tilde{D}_{CL}^{-m}} \left\{ \tilde{V}_{\text{core}}^2 [1+300\tilde{\delta}_C(1-K)][1-2\tilde{\delta}_C(1-K)]\left(\frac{1}{G_1}+\frac{1}{G_2}\right) + \tilde{V}_{\text{core}}^2 \left[1+300\tilde{\delta}_C T\frac{(1-K)}{K}\right]\left[1+2\tilde{\delta}_C T\frac{(1-K)}{K}\right]\frac{1}{G_3} - 4Y_M \right\} \tag{92}$$

Similarly, Eq. (71) can be nondimensionalized to

$$\tilde{V}_{TL}^{2-m} = \frac{T\tilde{\delta}_C[1+\tilde{\delta}_C T(1-K)/K]}{X_M^2 \tilde{D}_{TL}^{-m}} \left\{ \tilde{V}_{\text{core}}^2 \left[1+300\tilde{\delta}_C T\frac{(1-K)}{K}\right] \left[1+2\tilde{\delta}_C T\frac{(1-K)}{K}\right]\left(\frac{1}{G_3}+\frac{1}{G_4}\right) + \tilde{V}_{\text{core}}^2 [1+300\tilde{\delta}_C(1-K)] [1-2\tilde{\delta}_C(1-K)]\frac{1}{G_2} - 4Y_M \right\} \tag{93}$$

In Eqs. (92) and (93), the modified Lockhart-Martinelli parameter, X_M, and the dimensionless group, Y_M, are, respectively, given by

$$X_M = \left[\frac{\left(\frac{dp}{dz}\right)_{SL}}{\left(\frac{dp}{dz}\right)_{M,\text{core}}} \right]^{1/2} \tag{94}$$

and

$$Y_M = \left[\frac{(\rho_L - \rho_{\text{core}})g}{\left(\frac{dp}{dz}\right)_{M,\text{core}}} \right] \tag{95}$$

Also, the dimensionless groups, G_1, G_2, G_3, and G_4 are given, respectively, by

$$G_1 = \tilde{\delta}_C[1-\tilde{\delta}_C(1-K)] \tag{96}$$

$$G_2 = \frac{(1+K)}{4} - \tilde{\delta}_C[1-\tilde{\delta}_C(1-K)] - \tilde{\delta}_C TK\left[1+\tilde{\delta}_C T\frac{(1-K)}{K}\right] \tag{97}$$

$$G_3 = \frac{(1+K)}{4K} - \frac{\tilde{\delta}_C}{K}[1-\tilde{\delta}_C(1-K)] - \tilde{\delta}_C T\left[1+\tilde{\delta}_C T\frac{(1-K)}{K}\right] \tag{98}$$

$$G_4 = \tilde{\delta}_C T\left[1+\tilde{\delta}_C T\frac{(1-K)}{K}\right] \tag{99}$$

where

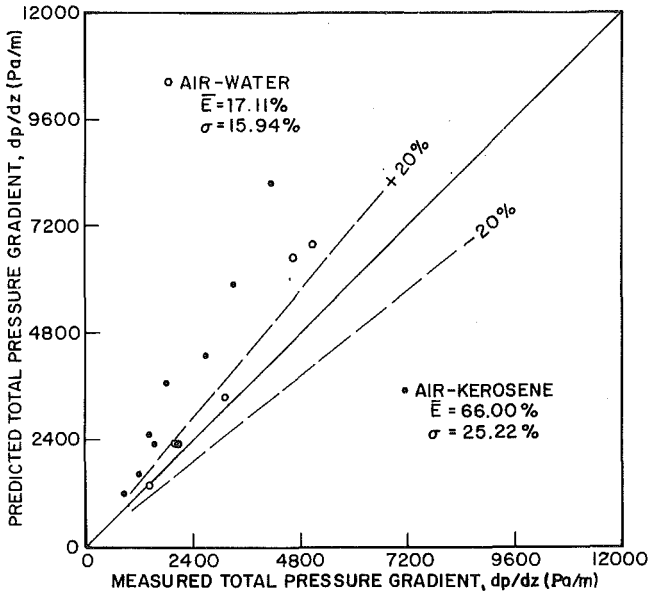

Fig. 19 Annular flow model performance—total pressure gradient in concentric annulus

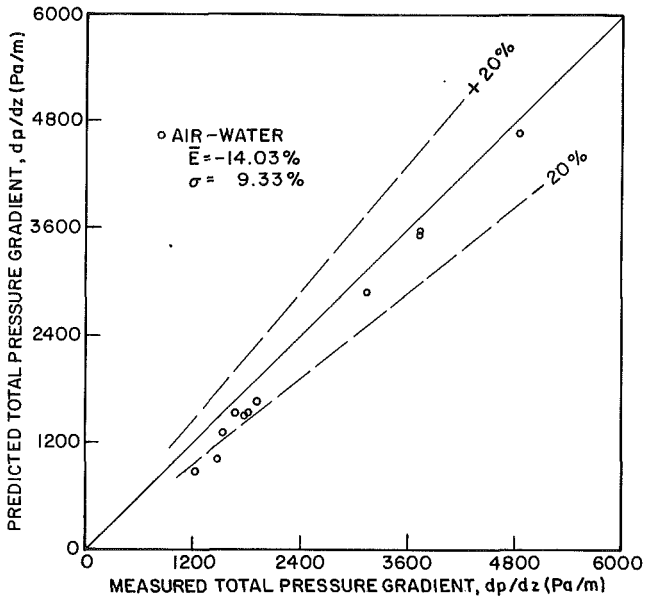

Fig. 20 Annular flow model performance—total pressure gradient in fully eccentric annulus

$$\tilde{\delta}_C=\frac{\delta_C}{D_H},\ \tilde{\delta}_T=\frac{\delta_T}{D_H},\ T=\frac{\tilde{\delta}_T}{\tilde{\delta}_C},\ \tilde{V}_{CL}=\frac{V_{CL}}{V_{SL}},$$

$$\tilde{V}_{TL}=V_{TL}/V_{SL},\ \tilde{V}_{\text{core}}=\frac{V_{\text{core}}}{V_{M,\text{core}}}\quad\text{and}\quad \frac{dp}{dz}\Big)_{SL},\ \frac{dp}{dz}\Big)_{M,\text{core}}$$

are the superficial pressure drop of the liquid phase and the core mixture, respectively. More details on the nondimensionalizing process can be found in Caetano (1985).

For a given set of input conditions, namely phase flow rates, fluid physical property values and configuration geometry, a solution is obtained for the set of equations constituting the model by using an iterative procedure on the casing liquid film thickness, $\tilde{\delta}_C$. Once the solution for the existing set of in-situ velocities and liquid holdups is found, the total pressure gradient can be determined by using the linear momentum equation written for any of the flow regions, namely casing liquid film, tubing liquid film and core, since the films are assumed stable.

Evaluation of Annular Flow Model. The model for annular flow developed in the previous section was used to predict the liquid holdup and total pressure gradient for the experimental flow conditions given in Tables 7 and 8. The performance of the model is obtained by comparing predicted and measured results.

Figures 17 and 18 show the model performance for the average volumetric liquid holdup predictions in the concentric and fully eccentric annulus configurations, respectively. Figures 19 and 20 show the respective model behavior for the total pressure gradient predictions. The model performance is considered reasonable for air-water in either annulus type. The model performance with air-kerosene is only fair.

The agreement between experimental results and the predictions of the annular model as compared to the models developed for the other flow patterns is less satisfactory. The experimental measurement accuracy obtained for the annular flow pattern must be considered. The quick-closing ball valves used to measure liquid holdup have a lower accuracy in annular flow than for all other flow patterns. This is due to the extremely low overall holdup values characteristic of annular flow. The reported holdup values were sometimes below the 3 percent minimum value possible to be measured. The pressure measurement system used may not be adequate for the cross-sectional and axial-dependent annular flow pattern. Also, due to the gas compressor limitations, it was not possible to acquire data covering the wider region in this flow pattern. A broader range of annular flow would provide a more representative evaluation of the average model performance.

A second major aspect in the model performance is its strong dependence on the entrained liquid fraction. If a larger fraction of entrained liquid is predicted, due to the existing high velocity in the core region a small overall liquid holdup value will be predicted. As reported by Wallis (1969), viscous liquids normally exhibit a smaller entrainment fraction than predicted by his correlation and used throughout the model. However, with the small amount of data acquired, it was not possible to introduce any correction to the correlation with regard to the viscous force magnitudes. For the same reason, no insights were obtained for the configuration geometry influence on entrained liquid fraction.

A third major aspect influencing the model performance is the film thickness ratio. The film thickness ratio became dependent on the adopted isotropy of scattering and independent of flow interference on the liquid droplets entrained in the gas core. The concept of isotropy was previously applied by Hutchinson et al. (1971). However, as reported by Garder (1975), the rate of deposition was found to be dependent on mechanisms which account for the existing flow field and are strongly determined by liquid droplet size.

These insights could not be used since no liquid droplet size measurements were performed in this investigation. As a result, a deposition rate expression was adopted which was a mass transfer process type and did not take into account the particle size and inherent type of deposition mechanism. Thus, in order to refine the model, more detailed characteristics data of this flow pattern are required.

Comprehensive Model

The modified flow pattern prediction model, and the models for bubble, slug, dispersed bubble and annular flow were incorporated into a comprehensive computer simulator for design purposes. A standard "marching" algorithm which numerically integrates the steady-state momentum equation for a given temperature profile is utilized. The existing flow pattern is first detected. The corresponding flow pattern model is then used to determine the flow characteristics. The overall

marching algorithm results in a computation of pressure and temperatures at calculation nodes in the wellbore annulus. Further discussion on this model is out of the scope of this paper.

Conclusions

Models based on two-phase flow mechanistic phenomena and incorporating annulus characteristics were developed for each of the existing flow patterns, namely, bubble, slug, dispersed bubble and annular flow. The models were tested against experimental data for average holdup and pressure gradient and showed good agreement, except for the annular flow pattern, where the agreement was fair. More detailed characteristics data of annuluar flow are required to refine the model for this flow pattern.

Acknowledgments

The authors wish to thank the Tulsa University Fluid Flow Projects (TUFFP) member companies for supporting this project. This paper was presented at the 4th International Conference on Multi-Phase Flow, organized by BHRA, in Nice, France, June 19–21, 1989. Copies of conference papers can be purchased from BHR Group.

References

Andersen, P. S., and Wurtz, J., 1981, "Adiabatic Steam-Water Annular Flow in an Annular Geometry," *International Journal of Multiphase Flow*, Vol. 7, pp. 235–239.

Angel, R. R., and Welchon, J. K., 1964, "Low-Ratio Gas-Lift Correlation for Casing-Tubing Annuli and Large-Diameter Tubing," *Drilling and Production Practices*, API, p. 100.

Barnea, D., and Brauner, N., 1985, "Holdup of the Liquid Slug in Two Phase Intermittent Flow," *International Journal of Multiphase Flow*, Vol. 11, pp. 43–49.

Baxendell, P. B., 1958, "Producing Wells on Casing Flow—An Analysis of Flowing Pressure Gradients," *AIME Trans.*, TP. 8027, pp. 202–206.

Caetano, F. E., 1985, "Upward Vertical Two-Phase Flow Through an Annulus," Ph.D. dissertation, The University of Tulsa.

Dukler, A. E., Wicks III, M., and Cleveland, R. G., 1964, "Frictional Pressure Drop in Two-Phase Flow: B. An Approach Through Similarity Analysis," *AIChE Journal*, Jan., Vol. 10, pp. 44–51.

Fernandez, R. C., Semiat, R., and Dukler, A. E., 1983, "Hydrodynamic Model for Gas-Liquid Slug Flow in Vertical Tubes," *AIChE Journal*, Vol. 9, No. 6, pp. 981–989.

Gaither, O. D., and Winkler, H. W., and Kirkpatrick, C. V., 1963, "Single and Two-Phase Fluid Flow in Small Diameter Vertical Conduits Including Annular Configurations," *Journal of Petroleum Technology*, Mar., pp. 309–320.

Gardner, G. C., 1975, "Deposition of Particles from a Gas Flowing Parallel to a Surface," *International Journal of Multiphase Flow*, Vol. 2, pp. 213–218.

Harmathy, T. Z., 1955, "Velocity of Large Drops and Bubbles in Media of Infinite or Restricted Extent," *AIChE Journal*, Vol. 1, pp. 289.

Hutchinson, P., and Whalley, P. B., 1973, "A Possible Characterization of Entrainment in Annular Flow," *Chemical Engineering and Science*, Vol. 28, pp. 974–975.

Hutchinson, P., Hewitt, G. F., and Dukler, A. E., 1971, "Deposition of Liquid or Solid Dispersions from Turbulent Gas Streams: A Stochastic Model," *Chemical Engineering and Science*, Vol. 26, pp. 419–439.

James, P. W., and Hutchinson, P., 1979, "Droplet Deposition in an Annular Geometry," *International Journal of Multiphase Flow*, Vol. 5, pp. 103–112.

McQuillan, K. W., and Whalley, P. B., 1985, "Flow Patterns in Vertical Two-Phase Flow," *International Journal of Multiphase Flow*, Vol. 11, pp. 161–175.

Nicklin, D. J., Wilkes, J. O., and Davidson, J. F., 1962, "Two-Phase Flow in Vertical Tubes," *Trans. of the Instn. of Chemical Engineers*, Vol. 40, pp. 61–68.

Ros, N. C. J., 1961, "Simultaneous Flow of Gas and Liquid as Encountered in Well Tubing," *Journal of Petroleum Technology*, Oct., pp. 1037–1049.

Sadatomi, M., Sato, Y., and Saruwatari, S., 1982, "Two-Phase Flow in Vertical Noncircular Channels," *International Journal of Multiphase Flow*, Vol. 8, pp. 641–655.

Salcudean, M., Chun, J. H., and Groeneveld, D. C., 1983, "Effect of Flow Obstructions on the Flow Pattern Transitions in Horizontal Two-Phase Flow," *International Journal of Multiphase Flow*, Vol. 9, pp. 87–90.

Salcudean, M., Groeneveld, D. C., and Leung, L., 1983, "Effect of Flow-Obstruction Geometry on Pressure Drops in Horizontal Air-Water Flow," *International Journal of Multiphase Flow*, Vol. 9, pp. 73–85.

Taitel, Y., Barnea, D., and Dukler, A. E., 1980, "Modelling Flow Pattern Transitions for Steady Upward Gas-Liquid Flow in Vertical Tubes," *AIChE Journal*, Vol. 26, pp. 345–354.

Wallis, G. B., 1969, *One-Dimensional Two-Phase Flow*, McGraw-Hill.

Whalley, P. B., and Hutchinson, P., 1981, "Comments on 'Adiabatic Steam-Water Flow in an Annular Geometry'," *International Journal of Multiphase Flow*, Vol. 7, pp. 241–243.

Whalley, P. B., 1977, "The Calculation of Dryout in a Rod Bundle," *International Journal of Multiphase Flow*, Vol. 3, pp. 501–515.

Winkler, H. W., 1968, "Single and Two-Phase Vertical Flow Through 0.996×0.625 inch Fully Eccentric Plain Annular Configuration," Ph.D. dissertation, The University of Texas at Austin.